ADVANCED ENERGY MATERIALS

Supporting Information

for *Adv. Energy Mater.,* DOI: 10.1002/aenm.202201608

Synchrotron Radiation Spectroscopic Studies of Mg^{2+} Storage Mechanisms in High-Performance Rechargeable Magnesium Batteries with Co-Doped FeS_2 Cathodes

Hao Xu, Yue Li, Dong Zhu, Zhao Li, Fengzhan Sun, Wen Zhu, Yu Chen, Jichao Zhang, Li Ren, Saihang Zhang, Jianxin Zou, and Richard M. Laine**

Supporting Information

Synchrotron Radiation Spectroscopic Studies of Mg^{2+} Storage Mechanisms in High-Performance Rechargeable Magnesium Batteries with Co-doped FeS_2 Cathodes

Hao Xu, Yue Li, Dong Zhu, Zhao Li, Fengzhan Sun, Wen Zhu, Saihang Zhang, Jianxin Zou and Richard M. Laine**

H. Xu, Z. Li, F. Z. Sun, W. Zhu, L. Ren, S. H. Zhang, Prof. J. X. Zou
National Engineering Research Center of Light Alloy Net Forming School of Materials Science and Engineering & State Key Laboratory of Metal Matrix Composites
School of Materials Science and Engineering
Shanghai Jiao Tong University
Shanghai, 200240, P. R. China
E-mail: zoujx@sjtu.edu.cn
H. Xu, Z. Li, F. Z. Sun, W. Zhu, L. Ren, S. H. Zhang, Prof. J. X. Zou
Center of Hydrogen Science
Shanghai Jiao Tong University
Shanghai, 200240, P. R. China
Y. Li
Shanghai Key Laboratory of Magnetic Resonance
School of Physics and Electronic Science
East China Normal University
Shanghai, 200241, P. R. China
D. Zhu
University of Chinese Academy of Science
Beijing, 100049, P. R. China
Y. Chen, J. C. Zhang
Shanghai Synchrotron Radiation Facility
Shanghai Advanced Research Institute
Chinese Academy of Sciences
Shanghai, 201204, P. R. China
Prof. R. M. Laine
Department of Materials Science and Engineering
University of Michigan, Ann Arbor
Michigan 48109-2136, United States
E-mail: talsdad@umich.edu

Experimental section

1. Preparation of Co-doped FeS_2

First, 4(1-*x*) mmol $FeSO_4 \cdot 7H_2O$ (99.9 %, Aladdin), 4*x* mmol $CoSO_4 \cdot 7H_2O$ (99.9 %, Aladdin), and 20 mmol urea (99.9 %, Aladdin) were added to a mixed solvent of 60 mL dimethylformamide (DMF, 99.9 %, Aladdin) and 80 mL ethylene glycol (EG, 99.9 %, Aladdin). After stirring for 10 minutes, 50 mmol sulfur (99.9 %, Aladdin) were added to the suspension. The mixture was further stirred at room temperature for 30 minutes with a rotation speed of 500 rpm. Then, the mixed suspension was transferred into a 200 mL Teflon-lined stainless-steel autoclave and kept at 180 ℃ for 12 h followed by cooling naturally to room temperature. After rinsing in DMF and deionized water to remove impurities and freeze-drying for two days, $Fe_{1-x}Co_xS_2$ (x=0, 0.1, 0.25, 0.5) powders were collected.

2. Preparation of electrolytes

Phenolate-based magnesium complex (PMC) electrolyte was prepared in a glove box filled with argon (both O_2 and H_2O contents were less than 0.01 ppm) at room temperature. First, 0.1333 g anhydrous $AlCl_3$ (99.99 %, Alfa Aesar) was dissolved in 2 mL anhydrous tetrahydrofuran (THF, 99.99 %, TCI) followed by stirring for 12 h at 500 rpm to obtain 0.5 mol L^{-1} $AlCl_3$/THF solution. In the meantime, 0.3284 g 2-*tert*-butyl-4-methylphenol (99.9 %, Alfa Aesar) was added to 1 mL anhydrous THF followed by stirring for 2 h at 500 rpm. The prepared solution is denoted as R-PhOH/THF where R represents the group of 2-*tert*-butyl-4-methylphenol. Then, 1 mL ethyl magnesium chloride solution (2 mol L^{-1}, Aladdin) was added dropwise to the R-PhOH/THF solution, as well as producing a lot of bubbles and releasing a lot of heat. Subsequently, the obtained solution was stirred for another 10 h at 500 rpm to obtain R-PhOMgCl/THF solution. Finally, 2 mL $AlCl_3$/THF solution was mixed with 2 mL R-PhOMgCl/THF solution to make 0.25 mol L^{-1} $(R\text{-}PhOMgCl)_2\text{-}AlCl_3$/THF solution, which is the PMC electrolyte.

All phenyl complex (APC) electrolyte was also prepared in a glove box filled with argon (both O_2 and H_2O contents were less than 0.01 ppm) at room temperature. First, 0.1333 g anhydrous $AlCl_3$ (99.99 %, Alfa Aesar) was dissolved in 3 mL anhydrous tetrahydrofuran (THF, 99.99 %, TCI) followed by stirring for 12 h at 500 rpm. Then, $AlCl_3$/THF solution was mixed with 1 mL PhMgCl solution (2 mol L^{-1}, J&K) to make 0.25 mol L^{-1} APC [$(PhMgCl)_2$-$AlCl_3$/THF] electrolyte.

3. Electrochemical measurements

The coin-type cells (CR2032) were assembled in an argon-filled glove box with the content of O_2 and H_2O less than 0.01ppm. First, the as-obtained $Fe_{1-x}Co_xS_2$ (x=0, 0.1, 0.25, 0.5) samples, commercial CoS_2 (99.99 %, Aladdin) and sulfur (99.99 %, Aladdin) were mixed with PVDF and super P carbon black at the mass ratio of 7:2:1. Then N-methylpyrrolidone (NMP, 99.9 %, Aladdin) was added to the above mixtures to form a slurry, uniformly pasted on the surface of the copper foil for vacuum drying at 80 ℃ for 8 h. The average mass loading was 1-1.5 mg cm^{-2} in this study. Polished magnesium foils were made as anodes and commercial glass fibers (Whatman, GF/F) were posted as the separators.

A LAND CT2001A multichannel battery test system between 0.01 and 2.0 V vs. Mg^{2+}/Mg at 25 ℃ was used for the galvanostatic charge/discharge cycling tests. When the discharge capacity is greater than 500 mAh g^{-1}, the number of cycles experienced by the battery is defined as the activation time. Thus, FeS_2, $Fe_{0.9}Co_{0.1}S_2$, $Fe_{0.75}Co_{0.25}S_2$ and $Fe_{0.5}Co_{0.5}S_2$ cathodes for RMBs show the activation time of 40, 39, 24 and 14 cycles, respectively. Besides, $Fe_{0.5}Co_{0.5}S_2$ cathodes after pre-charging for 2, 4 and 6 h show the activation time of 9, 6 and 5 cycles, respectively. Cyclic voltammetry (CV) tests at 0.1 mV s^{-1} and electrochemical impedance spectroscopy (EIS) measurements with amplitude of 5 mV and frequency between 100 kHz and 0.01 Hz were implemented on an electrochemical workstation (CHI 760E, Chenhua). Besides, measuring the stability of PMC electrolyte on stainless steel (SS) and Mg stripping/plating were also performed in coin-type cells (CR2032).

4. Material characterizations

X-ray diffraction (XRD) of samples was implemented on a Rigaku Smart Lab diffractometer with a Cu-K_α radiation (λ=1.5406Å) at a scanning rate of 2° min^{-1}. The morphologies were examined by scanning electron microscopy (SEM, Mira3 LHM), transmission electron microscopy (TEM, Talos F200X). Energy dispersive X-ray (EDX) spectrometer was attached on SEM. High resolution transmission electron microscopy (HRTEM) images, selected area electron diffraction (SAED) patterns and (high-angle annular dark-field) HAADF-(scanning transmission electron microscopy) STEM images were performed on a Talos F200X microscopy with an accelerating voltage of 200 kV. Chemical bonding analyses were examined by Fourier transform infrared spectroscopy (FTIR, Nicolet iS5, Thermo Fisher Scientific Inc. U.S.A.) equipped with a horizontal ATR accessory (Germanium crystal). Raman spectra were collected using an inVia Qontor confocal Raman microscope (Renishaw). ^{1}H and ^{27}Al Nuclear magnetic resonance (NMR) spectra were collected using a Bruker Avance NEO 700 MHz spectrometer. ^{25}Mg-NMR spectra were collected using a Bruker Avance NEO 600 MHz spectrometer. Differential scanning calorimetry (DSC) and thermal gravimetric (TGA) analyses were performed on an apparatus (Netzsch STA449F3 Jupiter) under flowing argon atmosphere with a heating rate of 5 °C min^{-1}. The nitrogen adsorption/desorption isotherms were obtained on a gas sorption analyzer (BELSORP-MAX) using Barrett-Joyner-Halenda methods. The elemental valence state was characterized by X-ray photoelectron spectroscopy equipped with a monochromated Al-Kα X-ray source (XPS, Ultra DLD, 1486.7 eV). 284.8 eV was used for C 1s as the reference to calibrate the XPS data. Besides, peak fitting was done using CASA XPS software. Electron paramagnetic resonance (EPR) was carried out at X-band (9.64 GHz) with a Brüker EMXplus-9.5/12 spectrometer.

The cathodes of cells after cycling tests were dismantled in the glove box with the content of water and oxygen both less than 0.1 ppm, then dried in the vacuum furnace at 30 ℃ for 2 h. The electrodes were then conducted in other measurements.

5. Synchrotron radiation spectroscopic studies

Soft X-ray absorption spectroscopy (sXAS) measurements of $Fe_{1-x}Co_xS_2$ (x=0, 0.1, 0.25, 0.5) samples were carried out at BL02B02 beamline of Shanghai Synchrotron Facility (SSRF). The spectra of Fe and Co L-edge were collected in TEY and TFY modes in an ultrahigh-vacuum chamber with a base pressure of about $5x10^{-10}$ Torr (1 Torr = 1.33322×10^2 Pa). The TEY and TFY spectra were normalized to the photon flux of incident beam monitored by the Au mesh.

The time-resolved reaction mechanisms of FeS_2 and $Fe_{0.5}Co_{0.5}S_2$ cathodes for RMBs under galvanostatic charge/discharge conditions were investigated by operando synchrotron X-ray diffraction (SXRD). For these tests, the positive/negative shells firstly pre-drilled were covered with Kapton films to facilitate the transmission of synchrotron radiation light and the isolation of air. The cells were assembled in an argon-filled glove box and installed on a square sample stage at the BL14B1 beamline of SSRF using a wavelength of 0.6887 Å. The size of beam was focused to 0.35×0.35 mm (vertical×horizontal). Diffraction data were collected on a CCD detector (Rayonix MX225, 3072 × 3072 pixels with 73 μm sides) every 21.7 s per image (including a 20 s photon counting time and 1.7 s response time). The two-dimensional X-ray scattering images were transformed to one-dimensional X-ray diffraction plot using Fit2d software.

The X-ray absorption fine structure (XAFS) spectra were performed at BL11B beamline in SSRF. The beam current of the storage ring was 200 mA in a top-up mode. The incident photons were monochromatized by a Si(111) double-crystal monochromator, with an energy resolution $\Delta E/E \approx 1.4\times10^{-4}$. The rejection of higher harmonics was achieved by a pair of Rh-coated mirrors at 4 mrad. The spot size at the sample was ≈200 μm×250 μm (H×V). All samples were pelletized as disks of 12 mm diameter with about 1 mm thickness using lithium fluoride as binder. The Fe K-edge XAS spectra were recorded at room temperature in the transmission mode, with the ionization chambers filled with N_2. The energy calibration was performed using a Fe

foil (7112 eV). The Co K-edge XAS spectra were recorded at room temperature in the transmission mode, with the ionization chambers filled with N_2. The energy calibration was performed using a Co foil (7709 eV). The acquired XAFS data were analyzed by Athena and Artemis software according to the standard procedures. The X-ray absorption near edge fine structure (XANES) spectra of dismantled electrodes were performed at BL15U beamline in SSRF. The acquired XANES data were analyzed by Athena software.

Supplementary figures

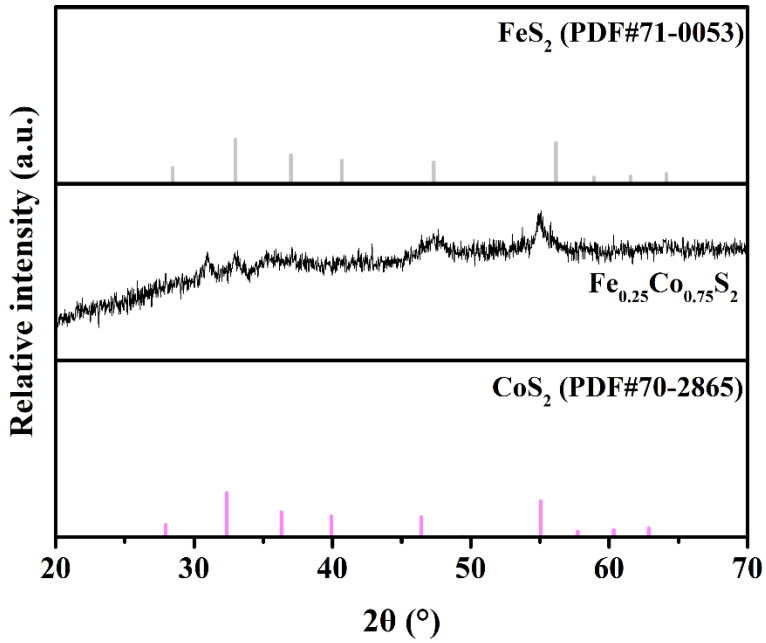

Figure S1. XRD pattern of as-prepared $Fe_{0.25}Co_{0.75}S_2$.

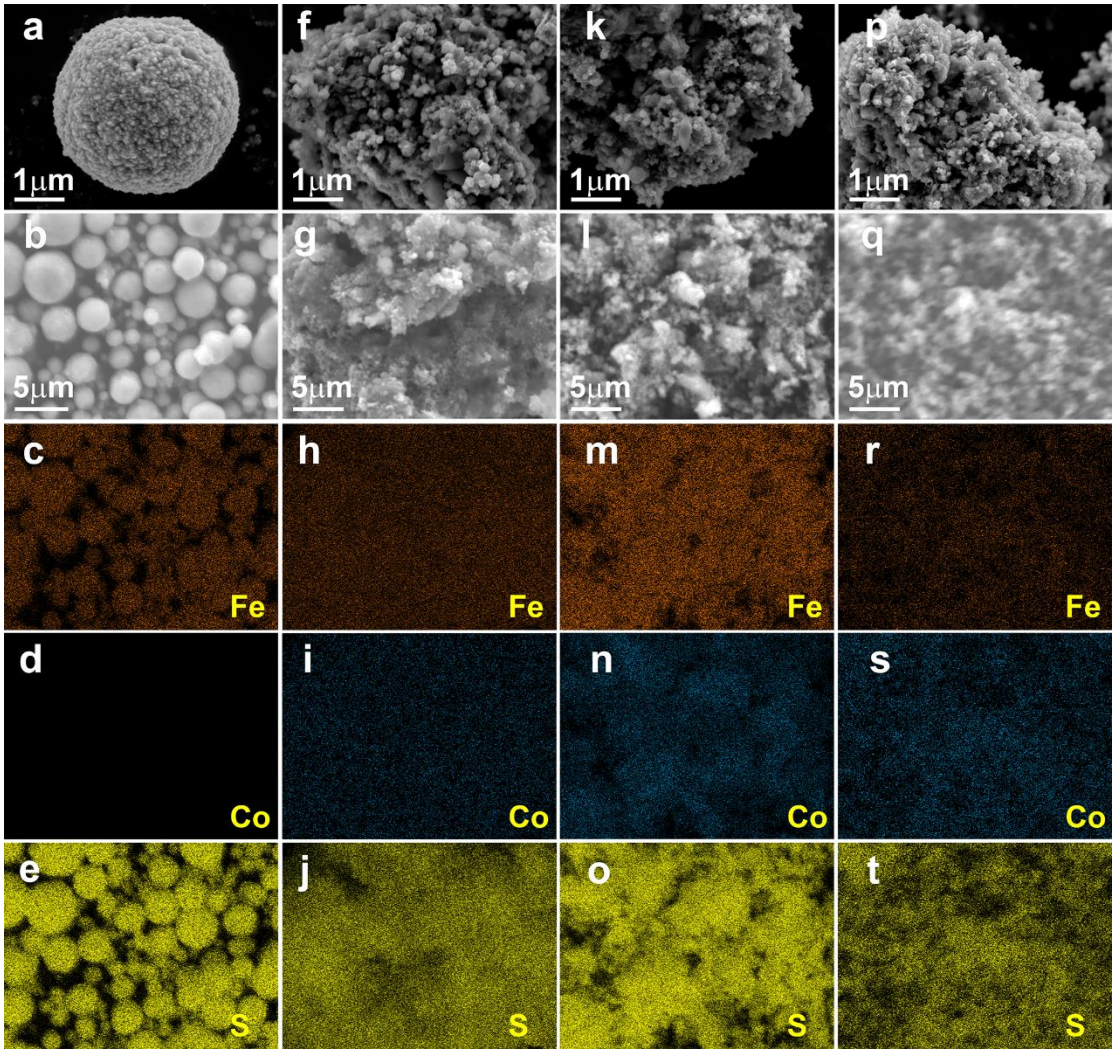

Figure S2. SEM images at different magnifications and EDX mapping results of as-prepared a-e) FeS_2, f-j) $Fe_{0.9}Co_{0.1}S_2$, k-o) $Fe_{0.75}Co_{0.25}S_2$ and p-t) $Fe_{0.5}Co_{0.5}S_2$ samples.

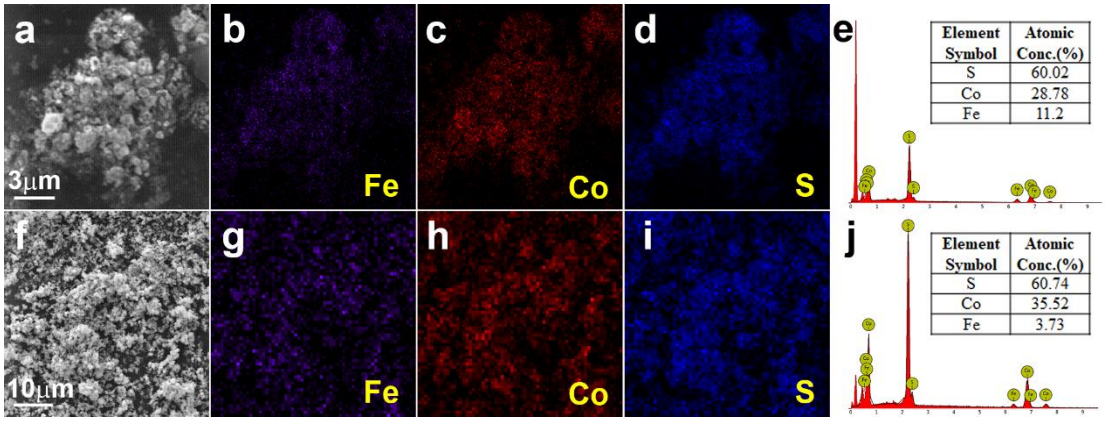

Figure S3. Typical SEM images at different magnifications and EDX mapping results of as-prepared a-e) $Fe_{0.25}Co_{0.75}S_2$ and f-j) $Fe_{0.1}Co_{0.9}S_2$ samples.

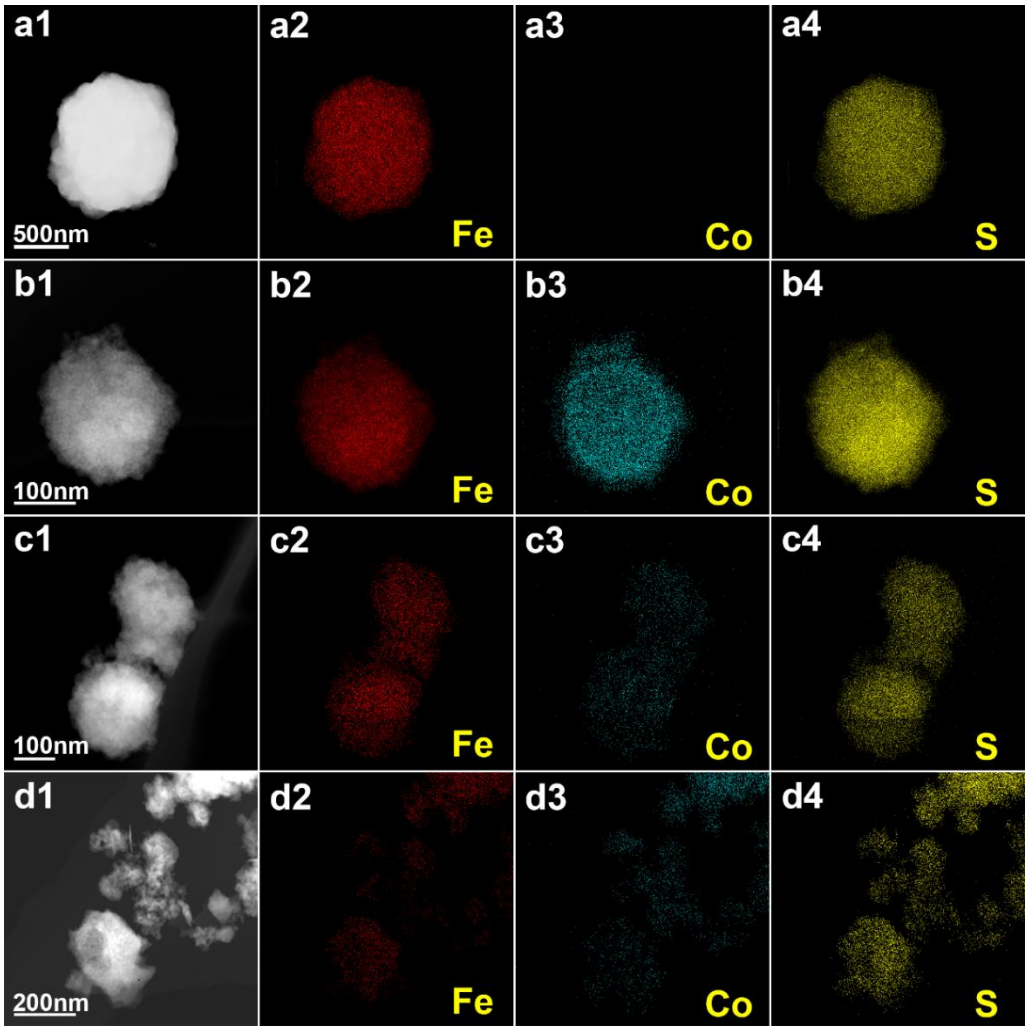

Figure S4. HAADF images and corresponding STEM mapping results of as-prepared a1-a4) FeS_2, b1-b2) $Fe_{0.9}Co_{0.1}S_2$, c1-c4) $Fe_{0.75}Co_{0.25}S_2$ and d1-d4) $Fe_{0.5}Co_{0.5}S_2$ samples.

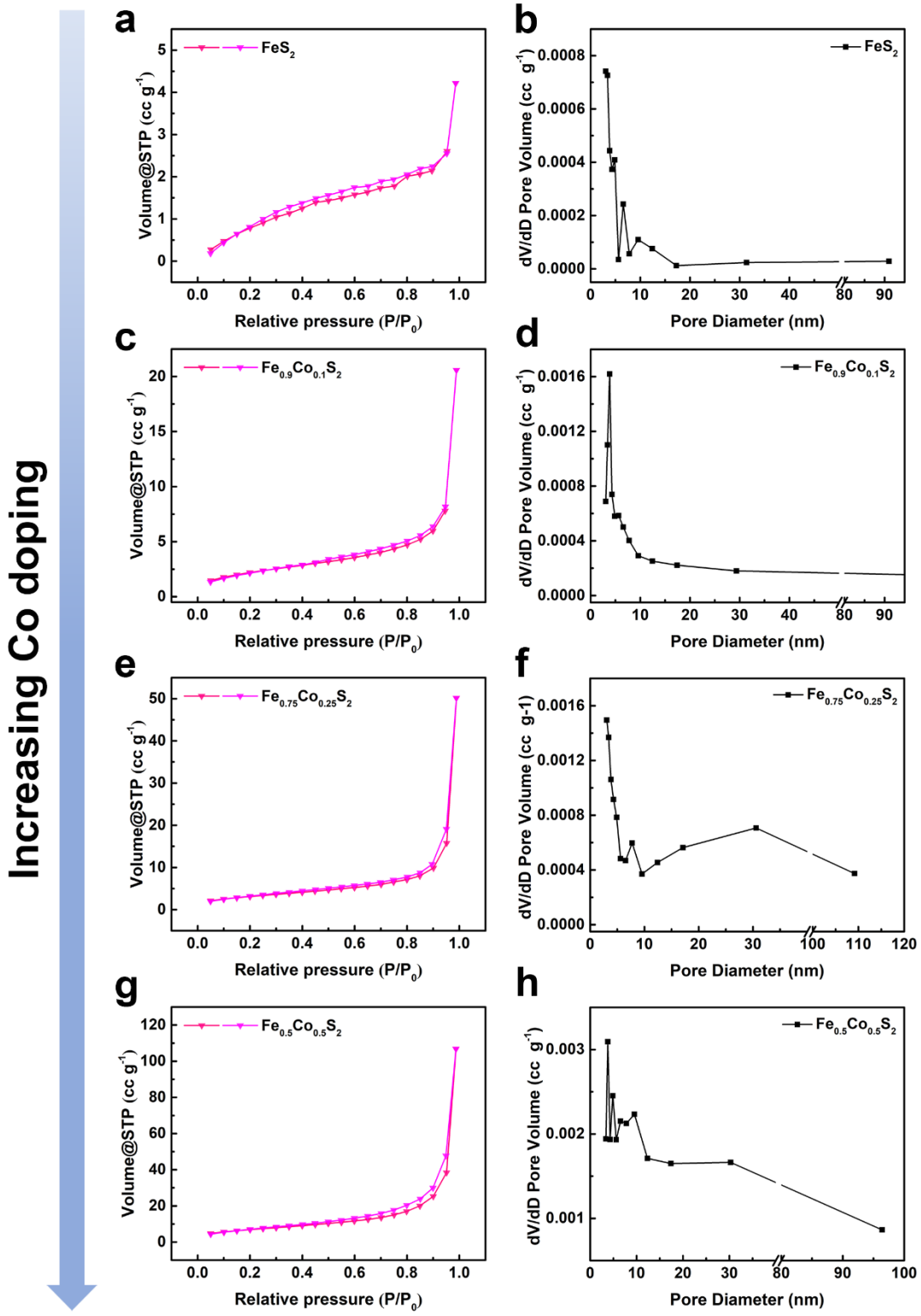

Figure S5. N_2 adsorption (red) and desorption (pink) isotherms of as-prepared a) FeS_2, c) $Fe_{0.9}Co_{0.1}S_2$, e) $Fe_{0.75}Co_{0.25}S_2$ and g) $Fe_{0.5}Co_{0.5}S_2$ samples. Pore size distributions of b) FeS_2, d) $Fe_{0.9}Co_{0.1}S_2$, f) $Fe_{0.75}Co_{0.25}S_2$ and h) $Fe_{0.5}Co_{0.5}S_2$ samples.

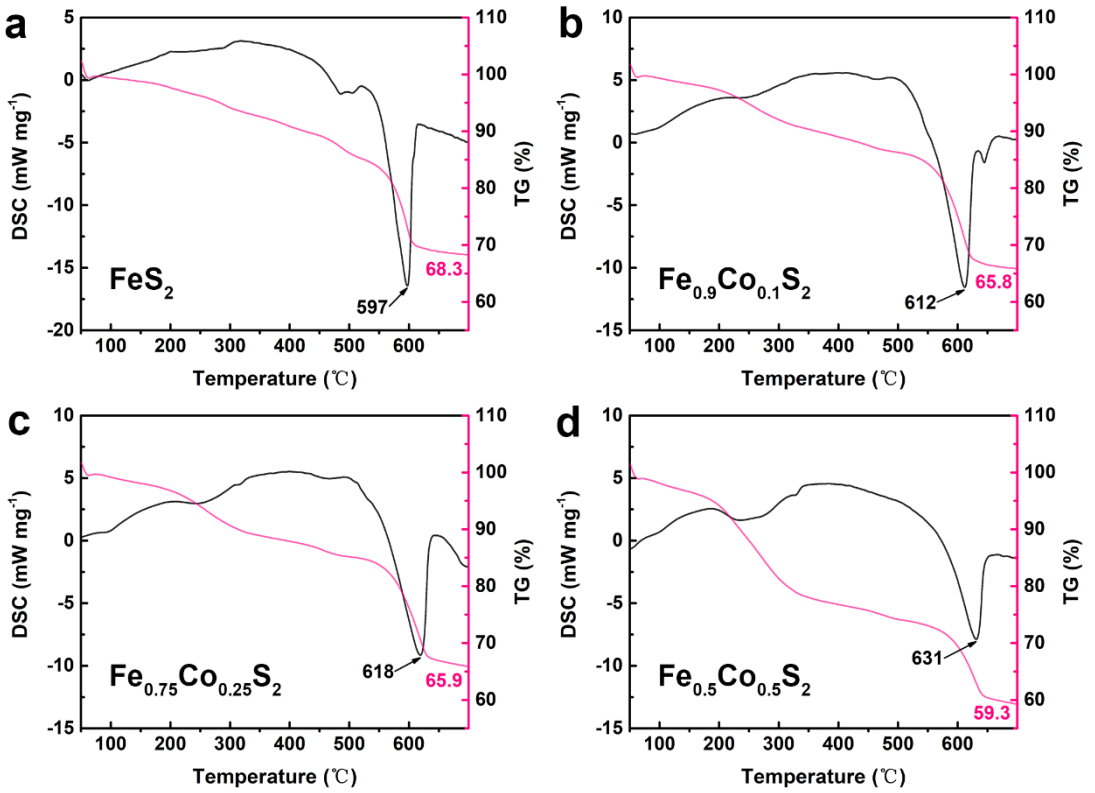

Figure S6. DSC curves and TGA profiles (5 °C min^{-1}) of as-prepared a) FeS_2, b) $Fe_{0.9}Co_{0.1}S_2$, c) $Fe_{0.75}Co_{0.25}S_2$ and d) $Fe_{0.5}Co_{0.5}S_2$ samples.

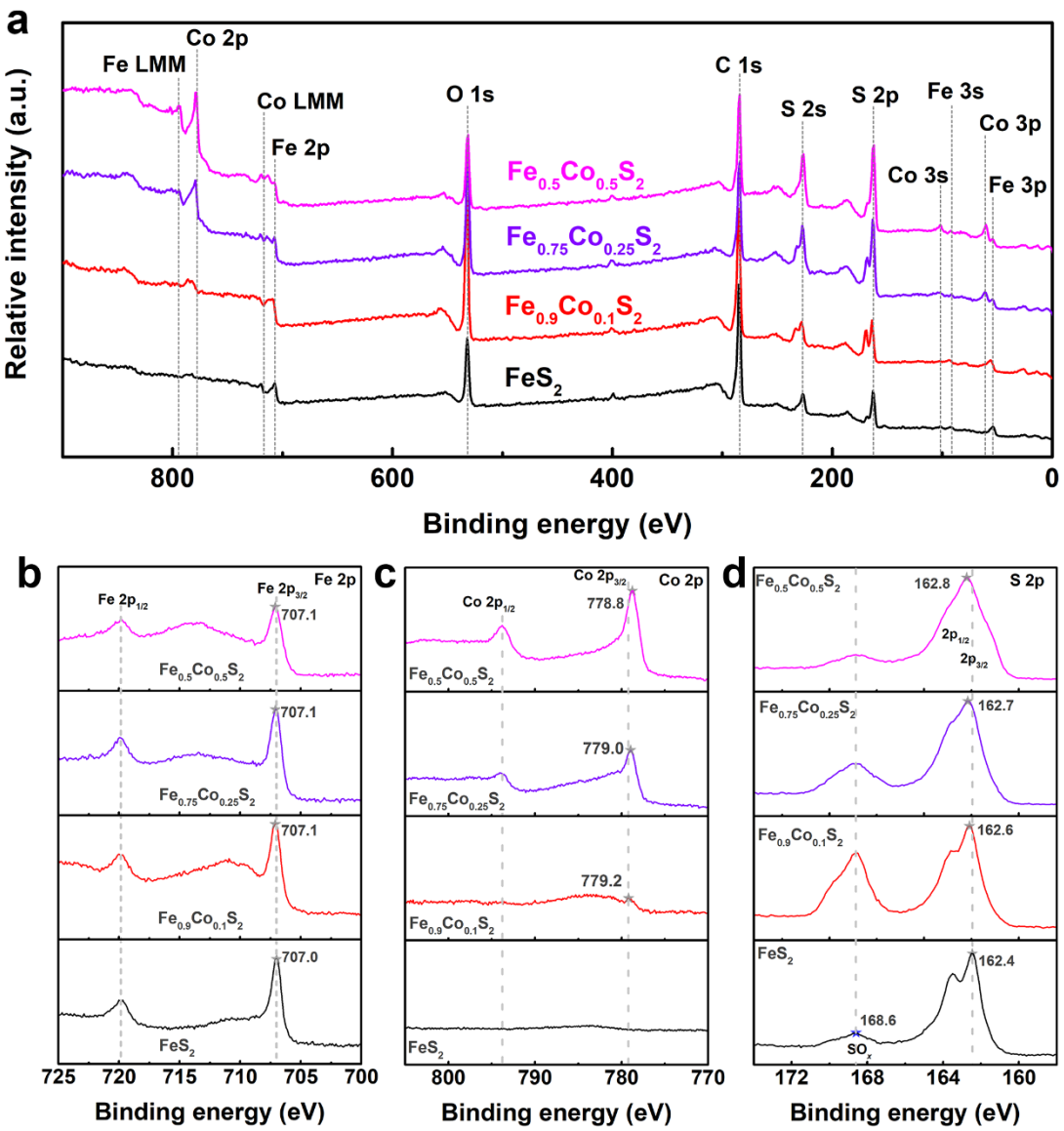

Figure S7. XPS spectra of as-prepared FeS_2, $Fe_{0.9}Co_{0.1}S_2$, $Fe_{0.75}Co_{0.25}S_2$ and $Fe_{0.5}Co_{0.5}S_2$ samples: a) survey spectra, b) Fe 2p, c) Co 2p and d) S 2p spectra.

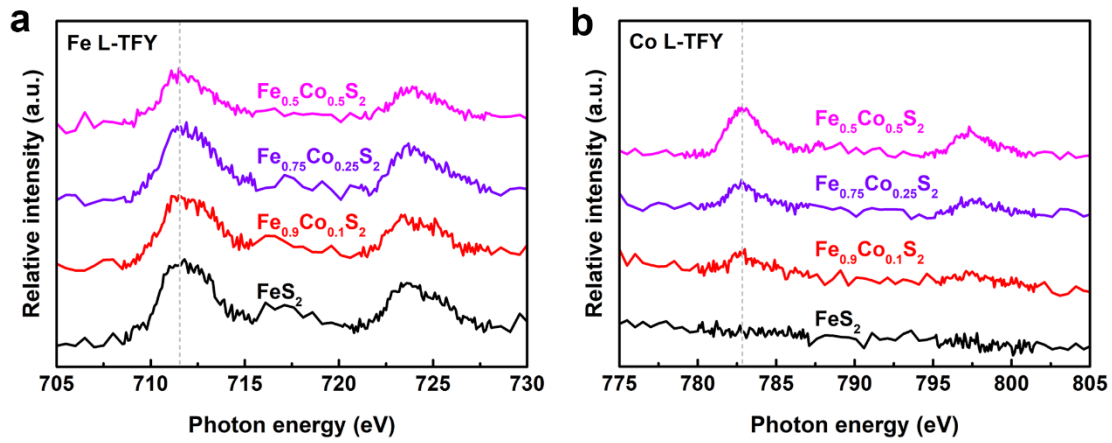

Figure S8. SXAS spectra of as-prepared FeS_2, $Fe_{0.9}Co_{0.1}S_2$, $Fe_{0.75}Co_{0.25}S_2$ and $Fe_{0.5}Co_{0.5}S_2$ samples: a) Fe L-TFY and b) Co L-TFY.

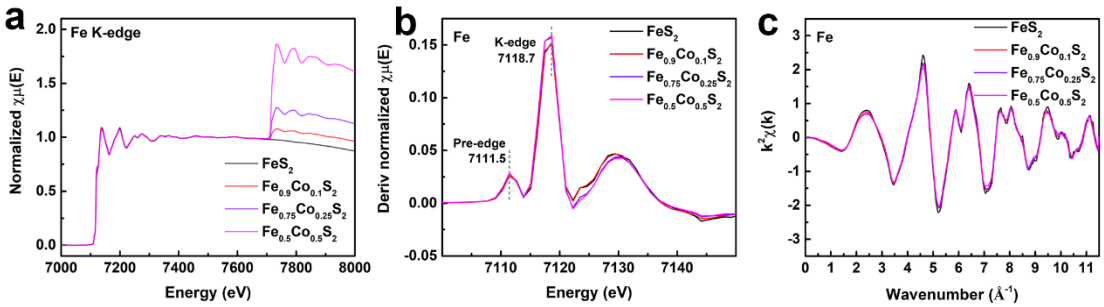

Figure S9. a) Fe K-edge XAFS spectra, b) first-derivative XANES plots and c) Fe K-edge EXAFS curves shown in k^2-weighted *k*-space for FeS_2, $Fe_{0.9}Co_{0.1}S_2$, $Fe_{0.75}Co_{0.25}S_2$ and $Fe_{0.5}Co_{0.5}S_2$ samples.

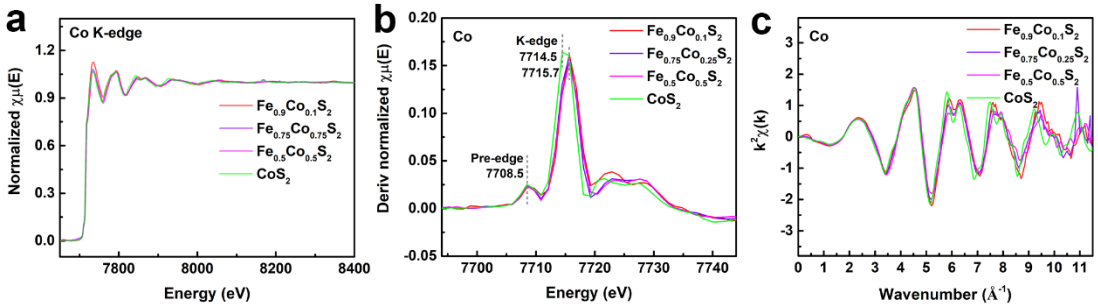

Figure S10. a) Co K-edge XAFS spectra, b) first-derivative XANES plots and c) Co K-edge EXAFS curves shown in *k*-space for $Fe_{0.9}Co_{0.1}S_2$, $Fe_{0.75}Co_{0.25}S_2$ and $Fe_{0.5}Co_{0.5}S_2$ and CoS_2 samples. The data are k^2-weighted and not phase-corrected.

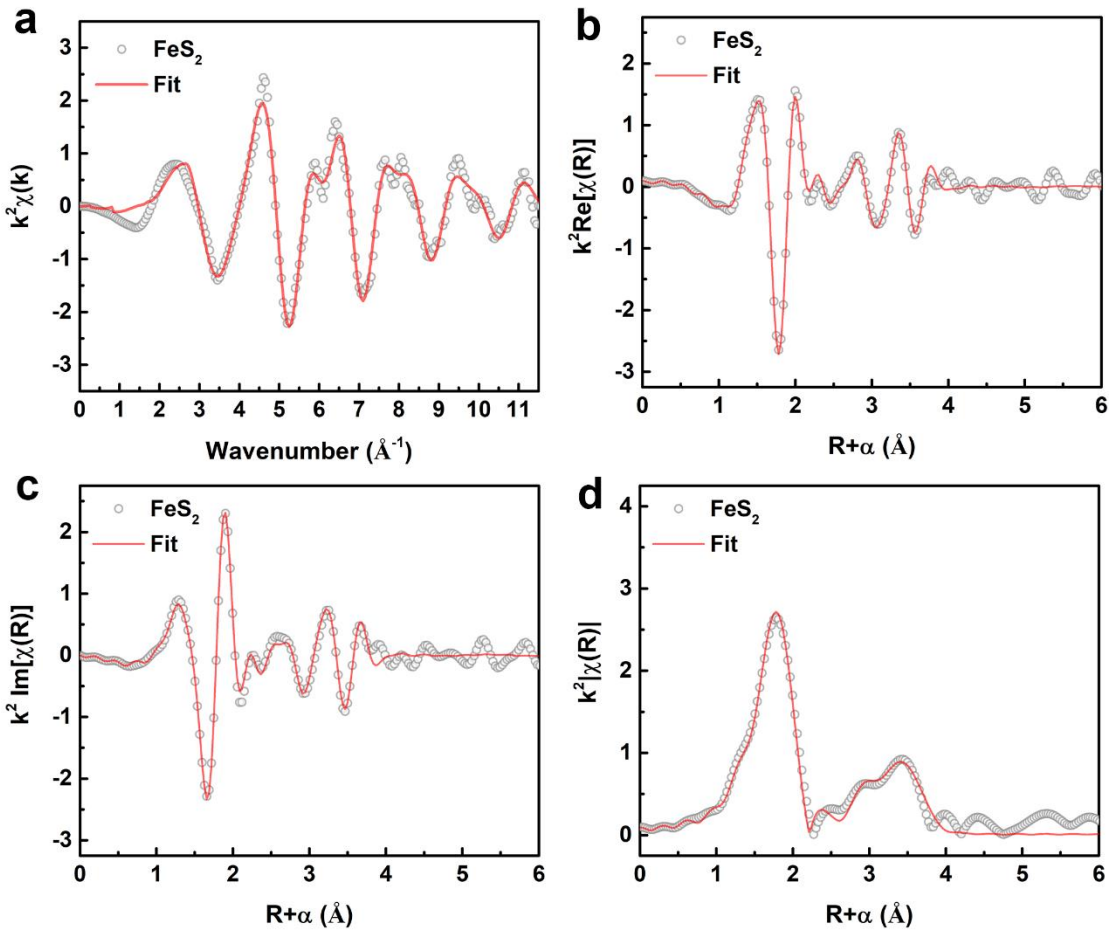

Figure S11. a) Fe K-edge EXAFS (points) and the curve fit (line) for FeS_2, shown in k-space. Fe K-edge EXAFS (points) and the curve fit (line) for FeS_2 shown in R-space, [b) real, c) imaginary and d) magnitude components, respectively]. The data are k^2-weighted and not phase-corrected.

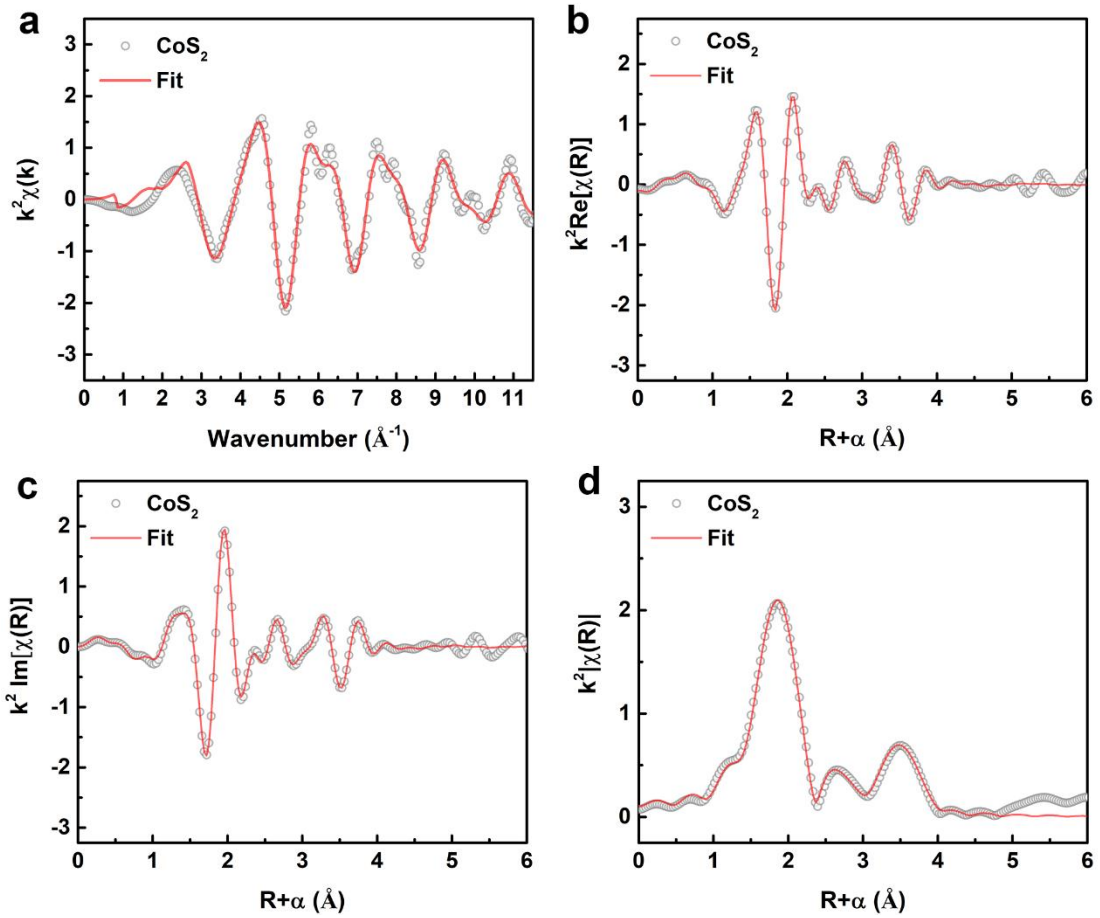

Figure S12. a) Co K-edge EXAFS (points) and the curve fit (line) for CoS_2, shown in k-space. Co K-edge EXAFS (points) and the curve fit (line) for CoS_2 shown in R-space, [b) real, c) imaginary and d) magnitude components, respectively]. The data are k^2-weighted and not phase-corrected.

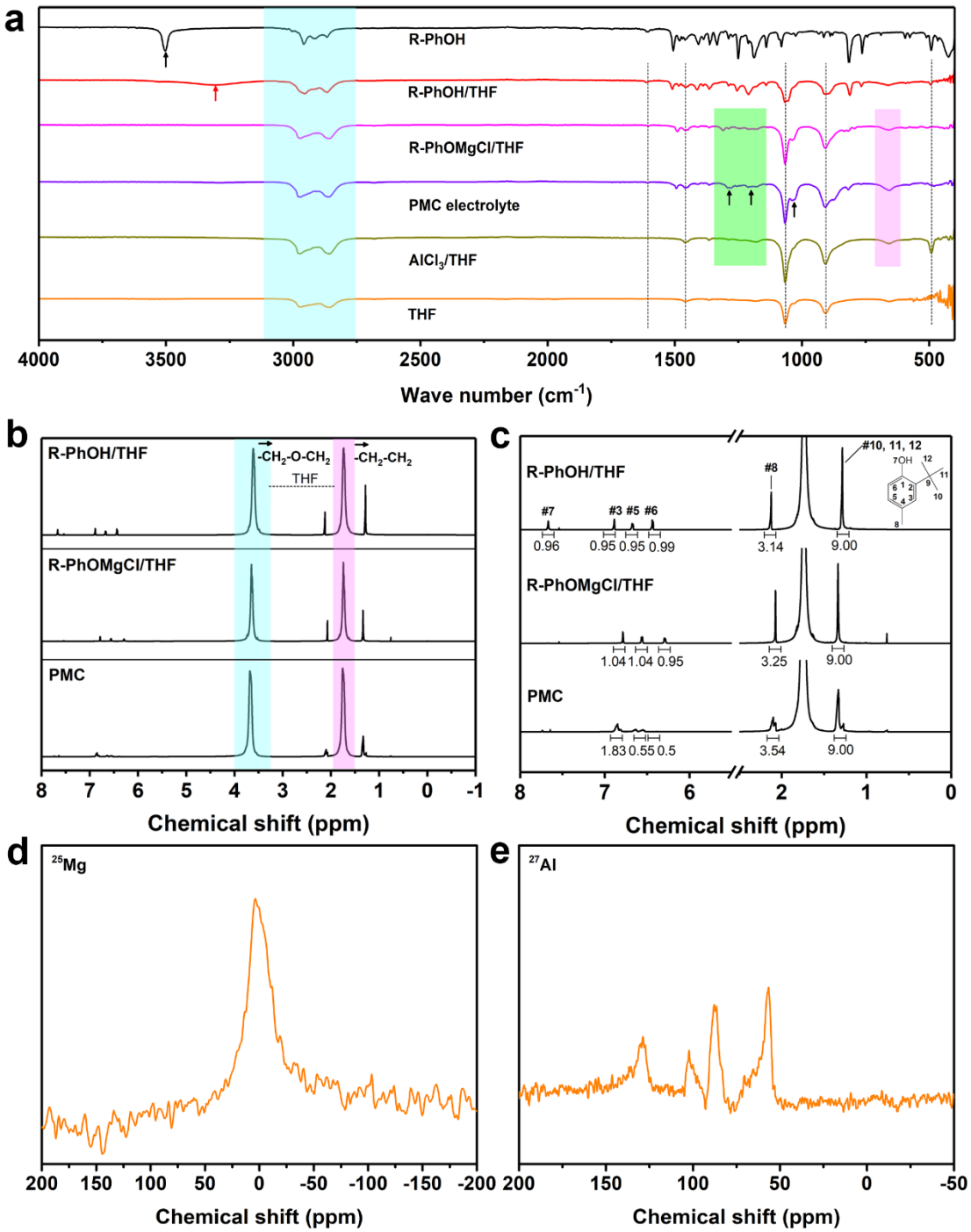

Figure S13. a) FTIR spectra of R-PhOH, R-PhOH/THF solution, R-PhOMgCl/THF solution, $(R\text{-}PhOMgCl)_2\text{-}AlCl_3$/THF (PMC) electrolyte, $AlCl_3$/THF solution and THF solvent. b, c) ^{1}H-NMR spectra of R-PhOH/THF solution, R-PhOMgCl/THF solution, PMC electrolyte. d) ^{25}Mg- and e) ^{27}Al-NMR spectra of PMC electrolyte.

Figure S13a shows the FTIR spectra of 2-*tert*-butyl-4-methylphenol (R-PhOH), 0.5 mol L^{-1} R-PhOH/THF solution, 0.5 mol L^{-1} R-PhOMgCl/THF solution, 0.25 mol L^{-1} $(R\text{-}PhOMgCl)_2\text{-}AlCl_3$/THF (PMC) electrolyte, 0.25 mol L^{-1} $AlCl_3$/THF solution and THF solvent. Most peaks can be attributed to THF: $\nu_{C\text{-}H}$ (3200-2800 cm^{-1}), $\delta_{C\text{-}H}$

(1460 cm^{-1}) and $\nu_{C\text{-}O}$ (1062 cm^{-1}) vibrational modes as well as $\delta_{C\text{-}C\text{-}O}$ bending (910 cm^{-1}), very consistent with the literature data.[1] R-PhOH shows a pronounced peak at 3504 cm^{-1}, related to $\nu_{O–H}$. When dissolved in THF, a wide and weak peak at 3307 cm^{-1} also belongs to $\nu_{O–H}$, indicating an interaction between R-PhOH and THF. However, after reacting with an equivalent of CH_3CH_2MgCl, the absorption related to $\nu_{O–H}$ is not observed in the spectrum of R-PhOMgCl/THF solution, indicating the full consumption of -OH and successful preparation.[2]

Besides, typical peaks for alkyl groups of R-PhOH ca. 3000-2800 cm^{-1} ($\upsilon_{C\text{-}H}$), 1470 and 1380 cm^{-1} $\delta_{C\text{-}H}$, overlap with THF vibrational modes. The appearance of peaks centered at 1605 cm^{-1} is attributed to $\nu_{C=C}$ of phenyl ring for R-PhOH, R-PhOH/THF solution, R-PhOMgCl/THF solution and PMC electrolyte.[3]

The spectrum of PMC electrolyte displays peaks (1350-1150 cm^{-1}) that can be ascribed to Al-O-C and Mg-O-C vibrational modes.[4] Moreover, this spectrum shows a small peak at 1033 cm^{-1}, ascribed to $\nu_{C\text{-}O}$ of THF coordinated with Mg^{2+} and Al^{3+}, which is also reflected in the spectrum of the R-PhOMgCl/THF solution. Moreover, the presence of a peak at 664 cm^{-1} could be ascribed to Al–O/Mg-O/Mg-Cl stretching models.[1a, 5]

We attribute the peak in the spectrum of the PMC electrolyte centered at 488 cm^{-1} to Al-Cl bonds, [1a] also reflected in the spectrum of $AlCl_3$/THF solution. These results indicate that THF molecules and Cl^- might coordinate with Mg^{2+} while R-PhO^- and Cl^- could coordinate with Al^{3+}.

NMR analyses were also performed, since multinuclear NMR spectroscopy had been demonstrated as a suitable technique for analyzing the chemical structure of Mg electrolyte solutions.[6] Structural analysis by ^{1}H-NMR was run on an Avance NEO NMR spectrometer (Bruker) in $CDCl_3$ solvent. Figure S13b, c show the ^{1}H-NMR spectra for R-PhOH/THF solution, R-PhOMgCl/THF solution and PMC electrolyte. It is obvious that R-PhOH and THF co-exist in R-PhOH/THF solution. After reacting with CH_3CH_2MgCl, the resulting PhOMgCl/THF solution shows few changes in terms of the number of different hydrogens on the benzene ring, demonstrating the retention of structure. Nevertheless, the ^{1}H-NMR spectrum of PMC electrolyte changes a lot and several new peaks appear, probably assignable to R-PhO^- coordinated with Al^{3+}.

^{25}Mg-NMR was performed on an Avance NEO NMR spectrometer (Bruker) in THF with chemical shifts reported relative to a solution of $MgCl_2$ in H_2O. Accordingly, the ^{25}Mg-NMR spectrum (Figure S13d) of PMC electrolyte shows a single sharp peak centered at 3.7 ppm, indicative of a single coordination environment, where magnesium is present as typically observed $[Mg_2(\mu\text{-}Cl)_3\bullet 6THF]^+$ complex cation.[7]

^{27}Al NMR was performed an Avance NEO NMR spectrometer (Bruker) in THF with chemical shifts reported relative to a solution of $AlCl_3$ in H_2O. The presence of multiple peaks in Figure S13e indicates that the Al species in the PMC electrolyte might consist of each species, $[Al(R\text{-}PhO)_{4-n}Cl_n]^-$ (n = 1–4).[8]

Combining these results and published data,[5, 7-8, 9] the active species in solutions consist of cations of $[Mg_2(\mu\text{-}Cl)_3\bullet 6THF]^+$ and anions of $[Al(R\text{-}PhO)_{4-n}Cl_n]^-$ (n = 1–4).

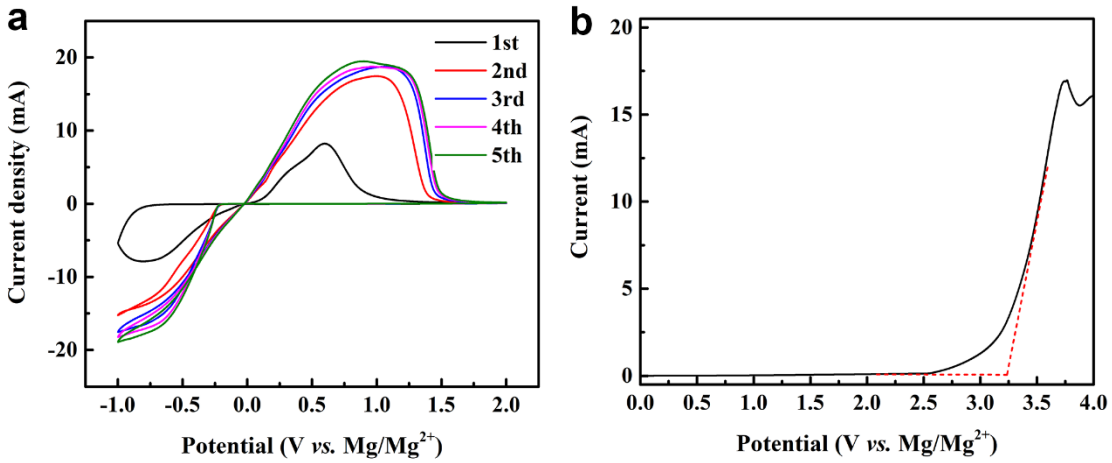

Figure S14. a) CV curves at 5 mV s^{-1} of Mg||PMC electrolyte||SS asymmetric batteries. b) LSV curves of PMC electrolyte at 10 mV s^{-1} during initial 5 cycles. The working electrodes were stainless steel (SS) foils with the counter and reference electrodes of Mg foils.

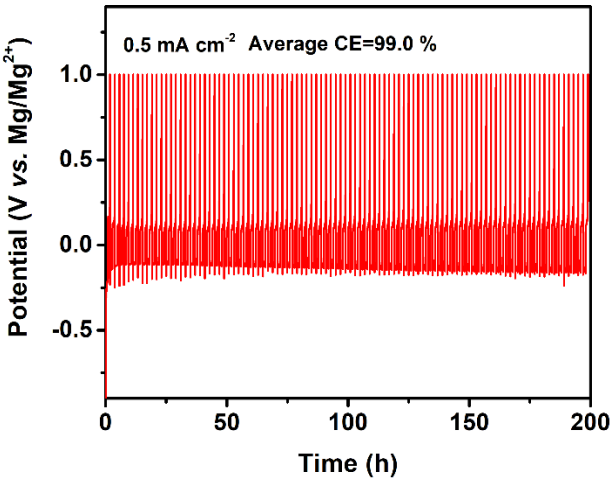

Figure S15. Coulombic efficiency of Mg stripping/plating during 100 cycles using Mg||PMC electrolyte||Cu cell at 0.5 mA cm^{-2}.

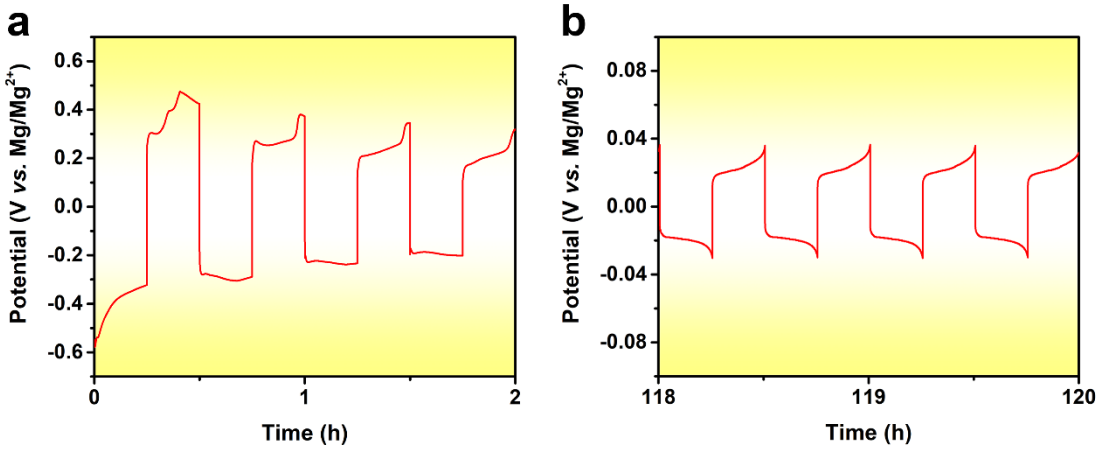

Figure S16. Mg stripping/plating behaviors of Mg||PMC electrolyte||Mg symmetric cells corresponding to Figure 4a: a) 0 to 2h and b) 118 to 120 h. The working, counter and reference electrodes of symmetrical cells are all Mg foils.

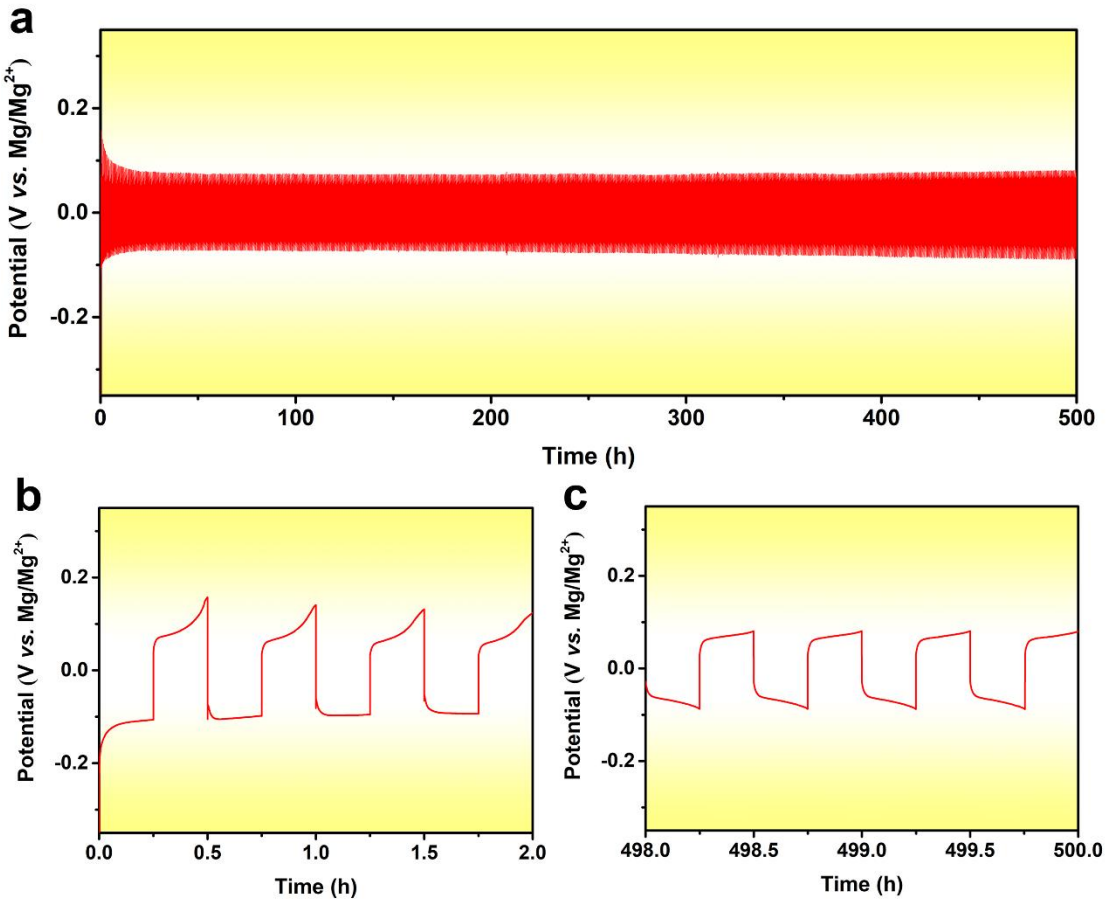

Figure S17. Mg stripping/plating behaviors of Mg||PMC electrolyte||Mg symmetric cells at 1 mA cm^{-2}: a) 0 to 500h, b) 0 to 2 h and c) 498 to 500 h. The working, counter and reference electrodes of symmetrical cells are all Mg foils.

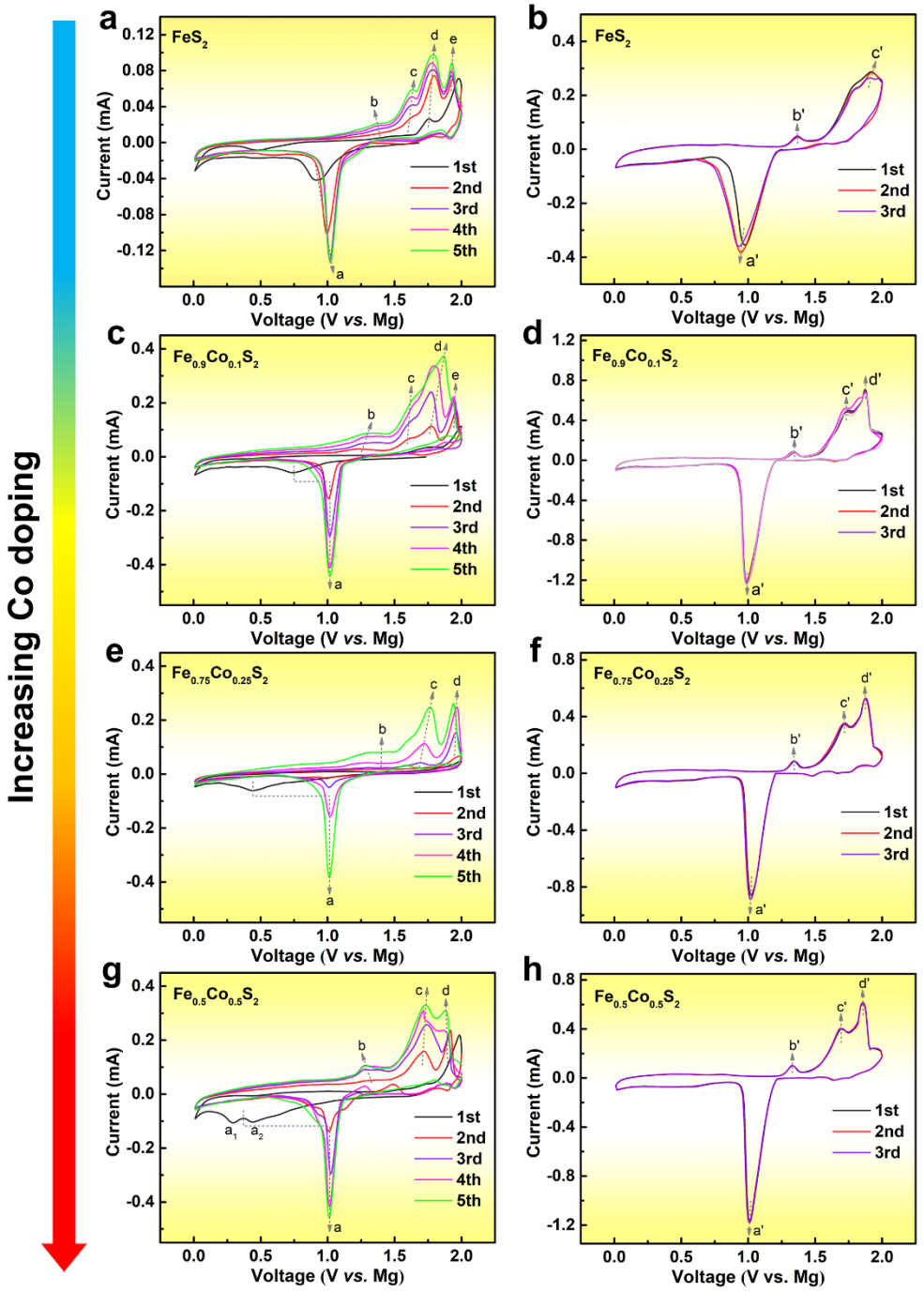

Figure S18. a) Cyclic voltammetry (CV) at 0.1 mV s^{-1} for the first five cycles and b) CV at 0.1 mV s^{-1} for the first three cycles of the FeS_2 cathodes cycled 50 times at 0.1 A g^{-1}. c) CV at 0.1 mV s^{-1} for the first five cycles and d) CV at 0.1 mV s^{-1} for the first three cycles of the $Fe_{0.9}Co_{0.1}S_2$ cathodes cycled 50 times at 0.1 A g^{-1}. e) CV at 0.1 mV s^{-1} for the first five cycles and f) CV at 0.1 mV s^{-1} for the first three cycles of the $Fe_{0.75}Co_{0.25}S_2$ cathodes cycled 50 times at 0.1 A g^{-1}. g) CV at 0.1 mV s^{-1} for the first five cycles and h) CV at 0.1 mV s^{-1} for the first three cycles of the $Fe_{0.5}Co_{0.5}S_2$ cathodes cycled 50 times at 0.1 A g^{-1}.

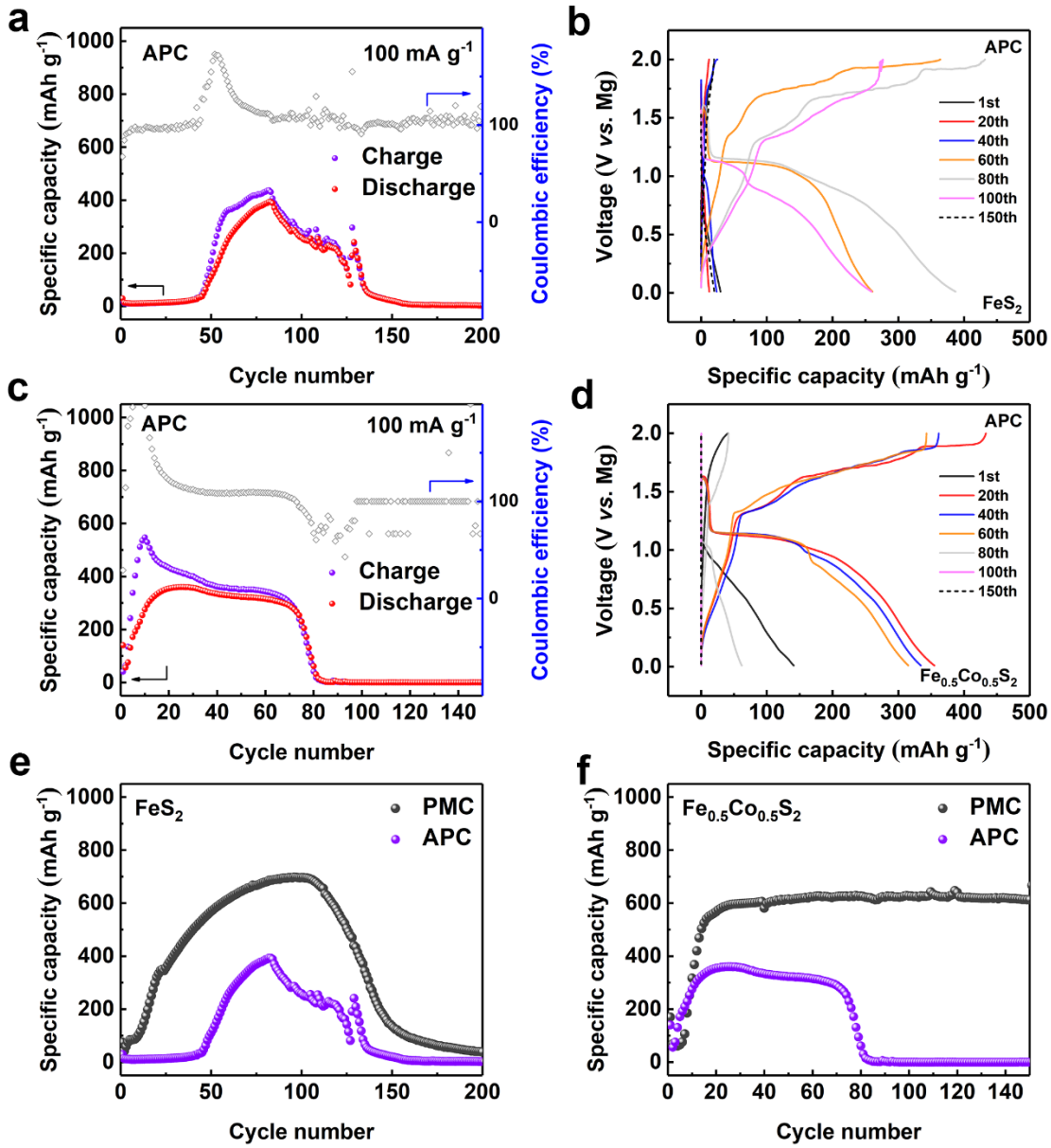

Figure S19. a) Cycling performance at 0.1 A g^{-1} and b) corresponding discharge/charge profiles during 1st, 20th, 40th, 60th, 80th, 100th and 150th cycles of FeS_2 cathodes for RMBs using the APC electrolyte. c) Cycling performance at 0.1 A g^{-1} and d) corresponding discharge/charge profiles during 1st, 20th, 40th, 60th, 80th, 100th and 150th cycles of $Fe_{0.5}Co_{0.5}S_2$ cathodes for RMBs using the APC electrolyte. Cycling performance comparison of e) FeS_2 and f) $Fe_{0.5}Co_{0.5}S_2$ cathodes for RMBs using different electrolytes.

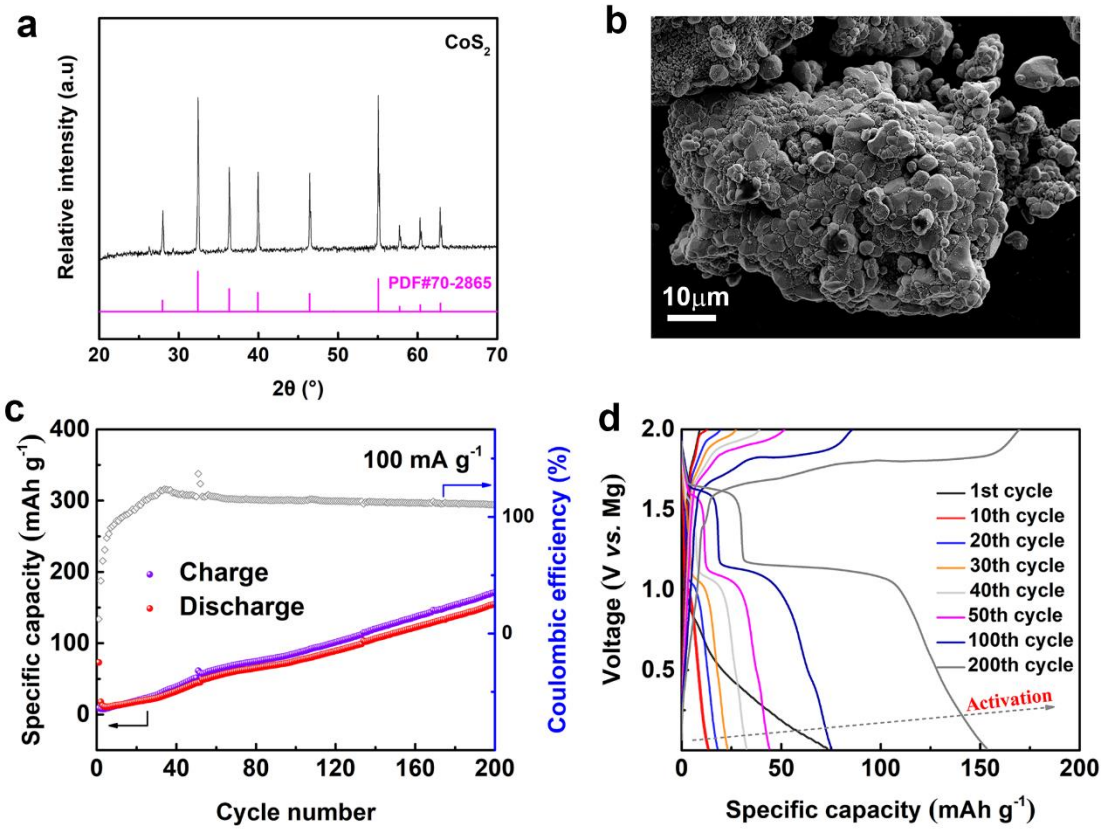

Figure S20. a) XRD pattern and b) SEM image of commercial CoS_2. c) Cycling performance at 0.1 A g^{-1} and d) corresponding discharge/charge profiles during 1^{st}, 10^{th}, 20^{th}, 30^{th}, 40^{th}, 50^{th}, 100^{th} and 200^{th} cycles of commercial CoS_2 cathodes for RMBs using PMC electrolyte and copper collectors.

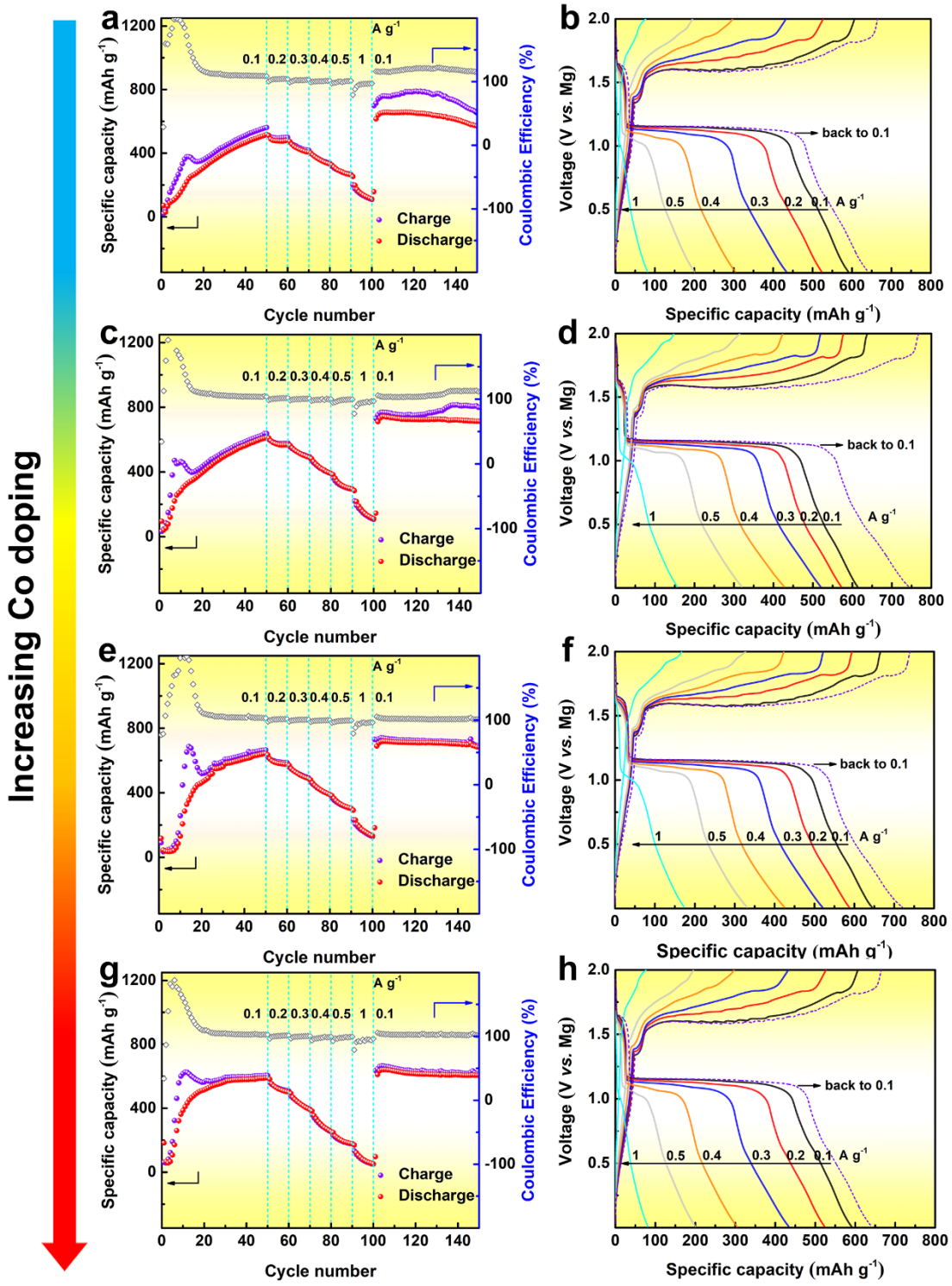

Figure S21. Rate performance at different current densities ranging from 0.1 to 1 A g^{-1} and the corresponding discharge/charge profiles of 5th cycle at each current density for a, b) FeS_2, c, d) $Fe_{0.9}Co_{0.1}S_2$, e, f) $Fe_{0.75}Co_{0.25}S_2$ and g, h) $Fe_{0.5}Co_{0.5}S_2$ cathodes of RMBs using PMC electrolyte and copper collectors.

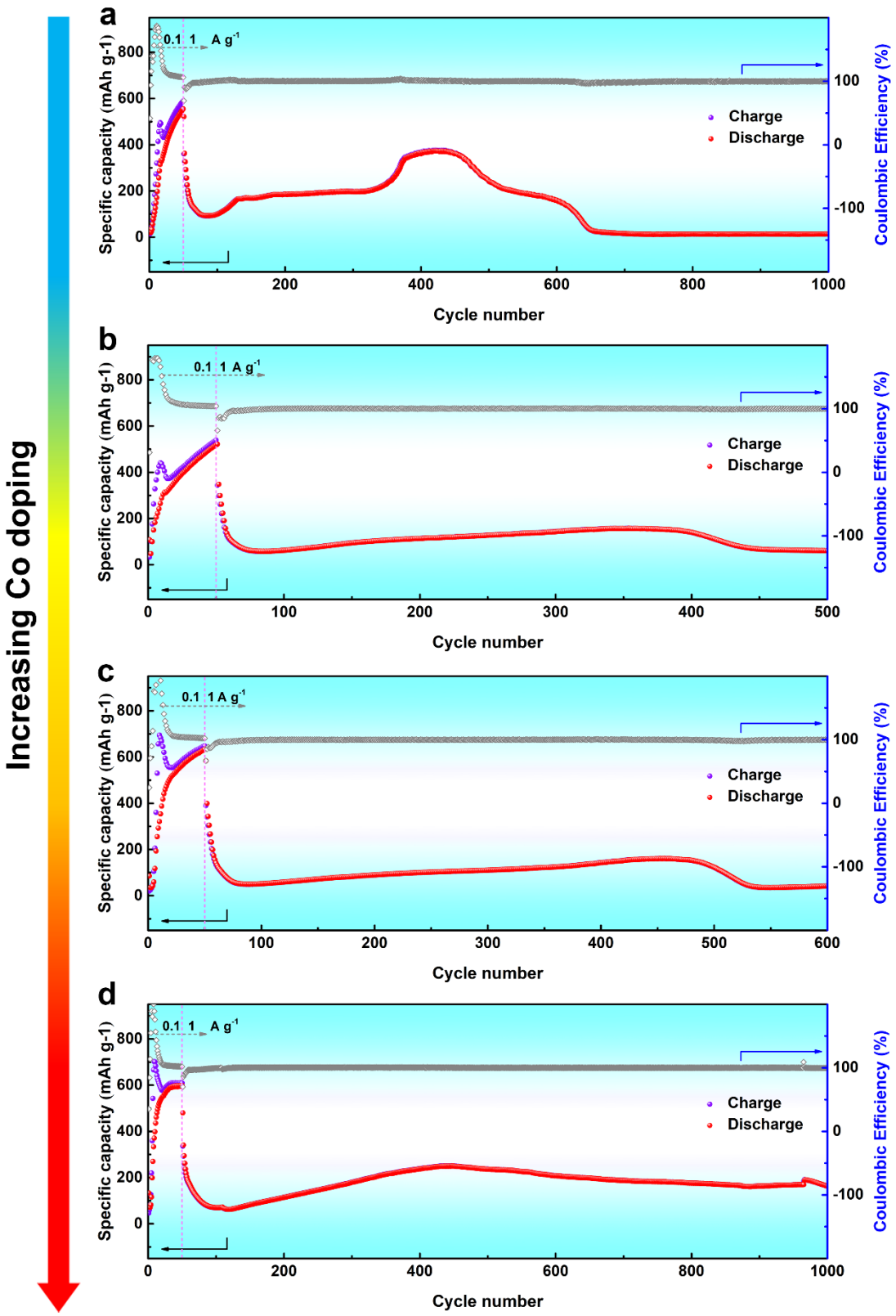

Figure S22. Cycling performance at 1 A g^{-1} of a) FeS_2, b) $Fe_{0.9}Co_{0.1}S_2$, c) $Fe_{0.75}Co_{0.25}S_2$ and d) $Fe_{0.5}Co_{0.5}S_2$ cathodes after cycling at 0.1 A g^{-1} for 50 times.

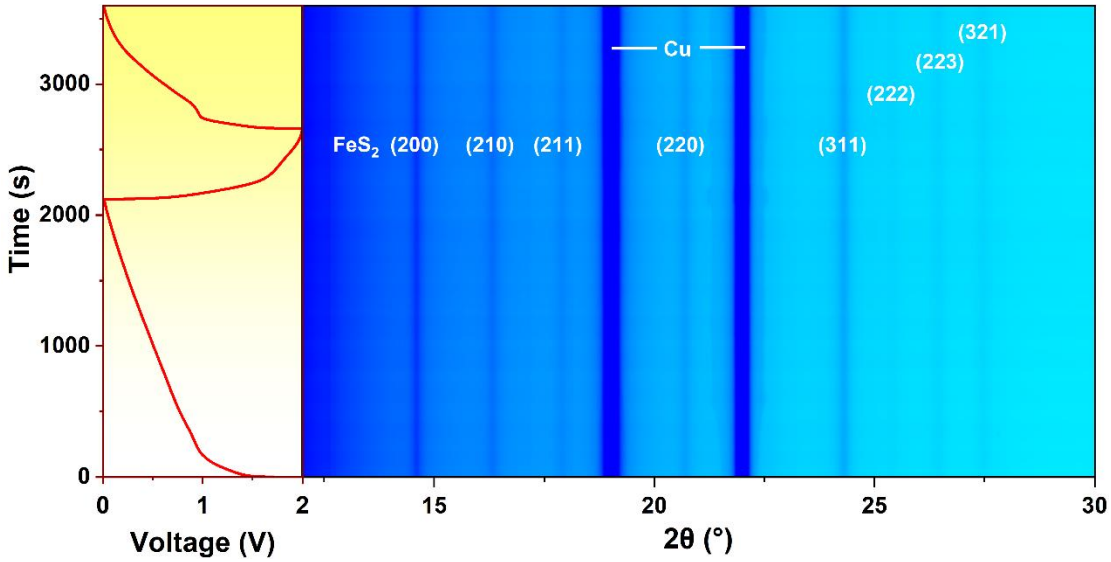

Figure S23. The voltage-time curve of FeS_2 cathodes coupling with PMC electrolyte and copper collectors for RMBs during initial cycling and corresponding operando SXRD counter plots.

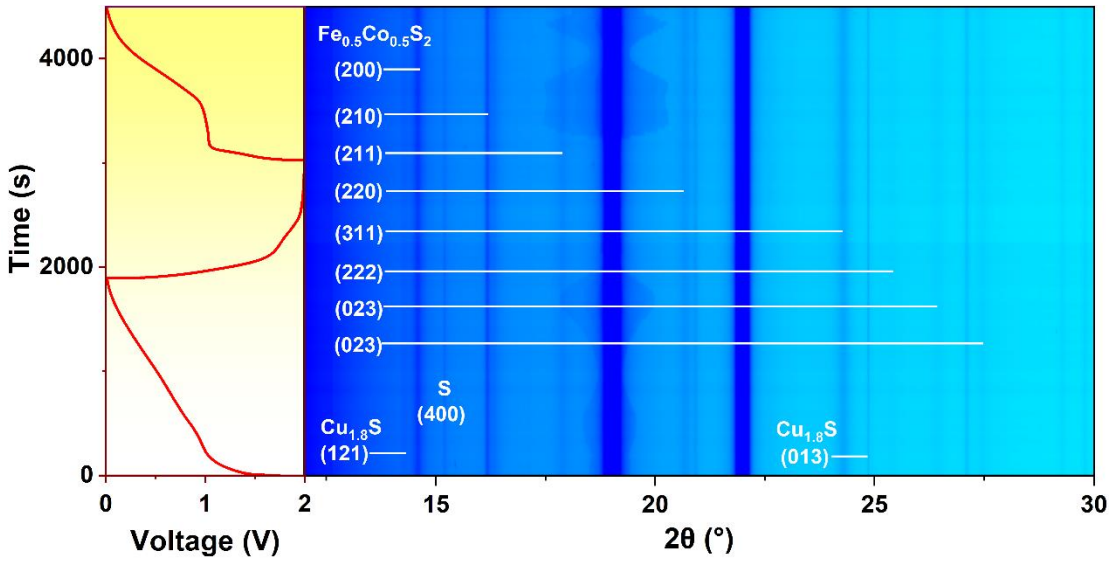

Figure S24. The voltage-time curve of $Fe_{0.5}Co_{0.5}S_2$ cathodes coupling with PMC electrolyte and copper collectors for RMBs during initial cycling and corresponding operando SXRD counter plots.

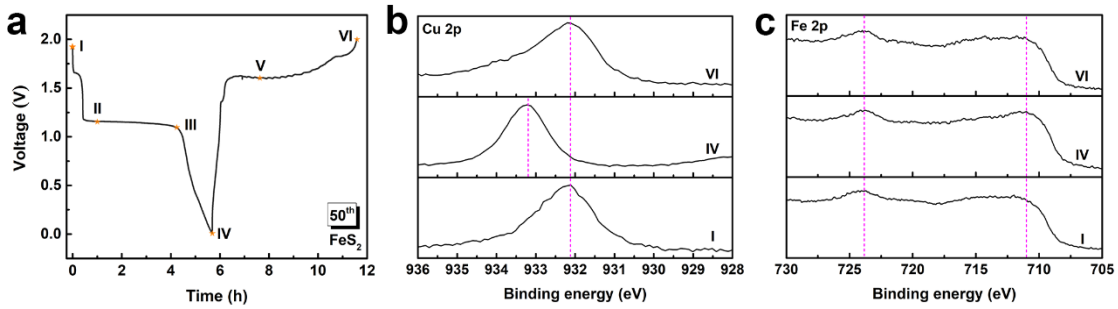

Figure S25. a) The voltage-time curve of FeS_2 cathodes coupling with PMC electrolyte and copper collectors for RMBs during 50^{th} cycle. b) Cu 2p and c) Fe 2p spectra of FeS_2 cathodes in different states (I, IV and VI).

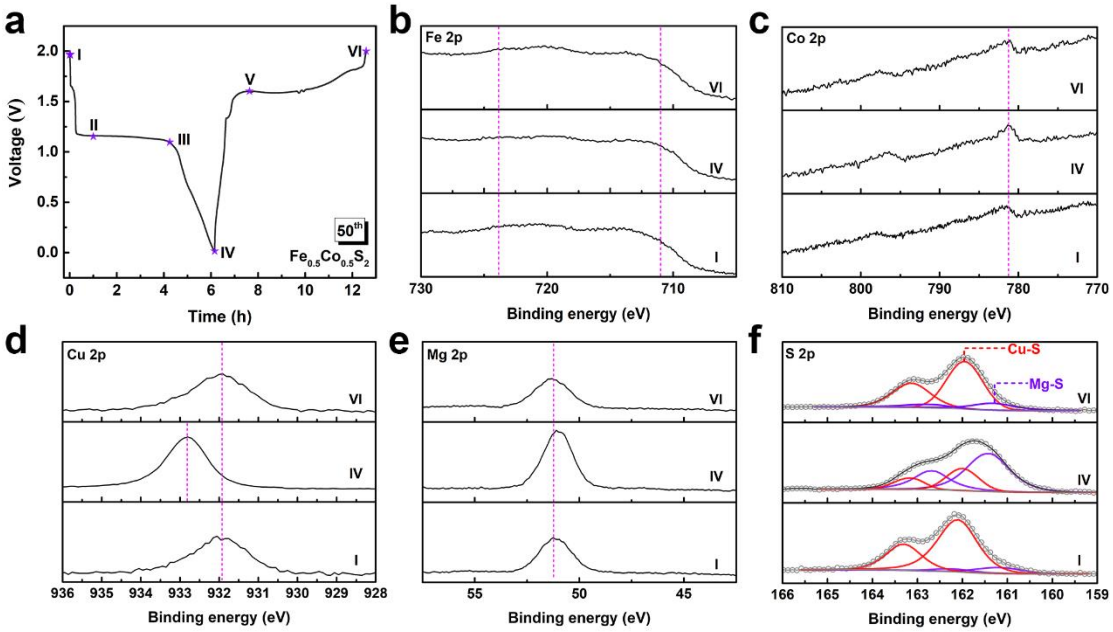

Figure S26. a) The voltage-time curve of $Fe_{0.5}Co_{0.5}S_2$ cathodes coupling with PMC electrolyte and copper collectors for RMBs during 50^{th} cycle. b) Fe 2p, c) Co 2p, d) Cu 2p, e) Mg 2p and f) S 2p spectra of $Fe_{0.5}Co_{0.5}S_2$ cathodes in different states (I, IV and VI).

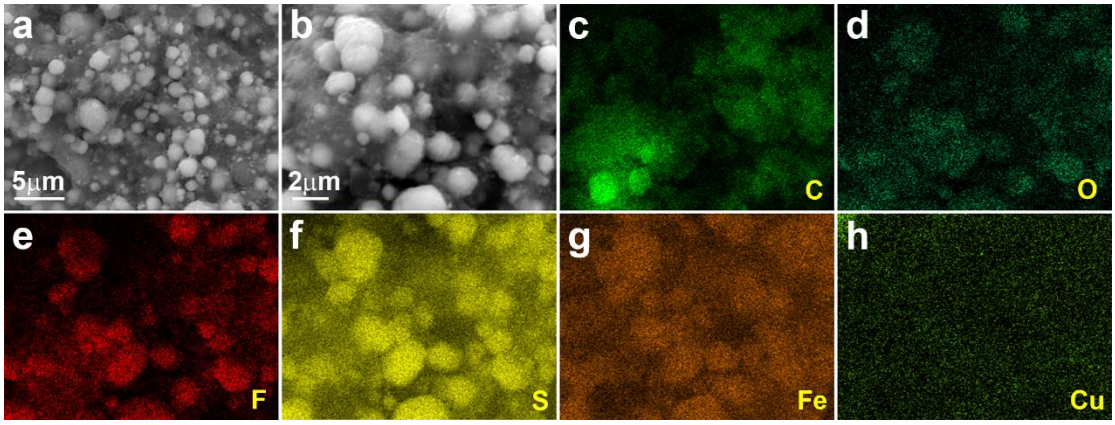

Figure S27. a, b) Typical SEM images at different magnifications of the pristine FeS_2 electrode and c-h) corresponding element mapping results.

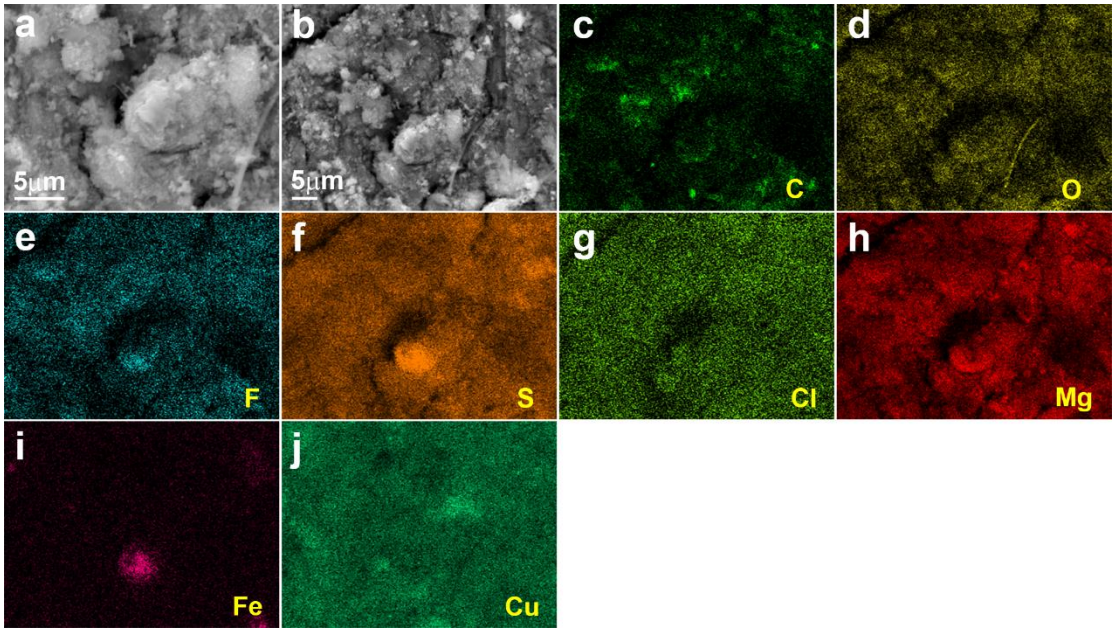

Figure S28. a, b) Typical SEM images at different magnifications of the FeS_2 electrode in fully discharged state (cycle 50) and c-j) corresponding element mapping results.

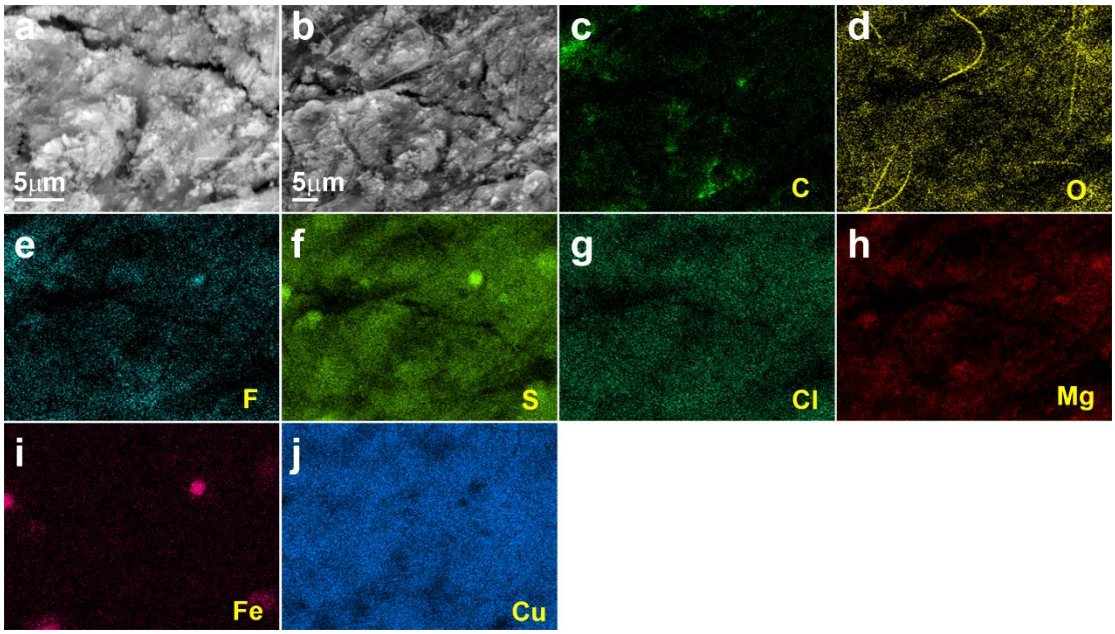

Figure S29. a, b) Typical SEM images at different magnifications of the FeS_2 electrode in fully charged state (cycle 50) and c-j) corresponding element mapping results.

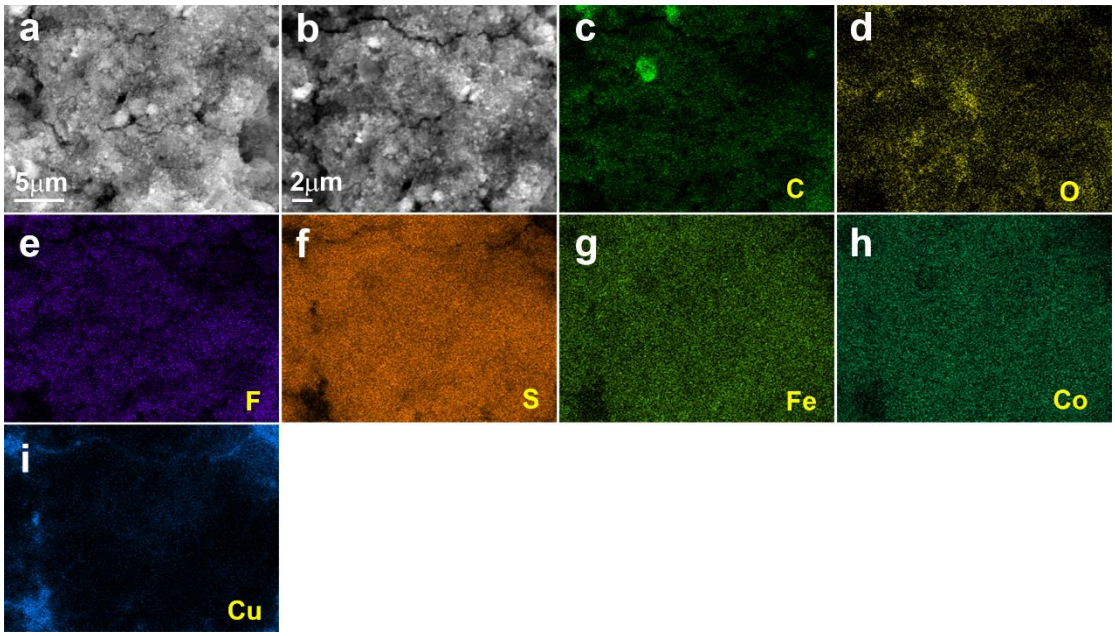

Figure S30. a, b) Typical SEM images at different magnifications of the pristine $Fe_{0.5}Co_{0.5}S_2$ electrode and c-i) corresponding element mapping results.

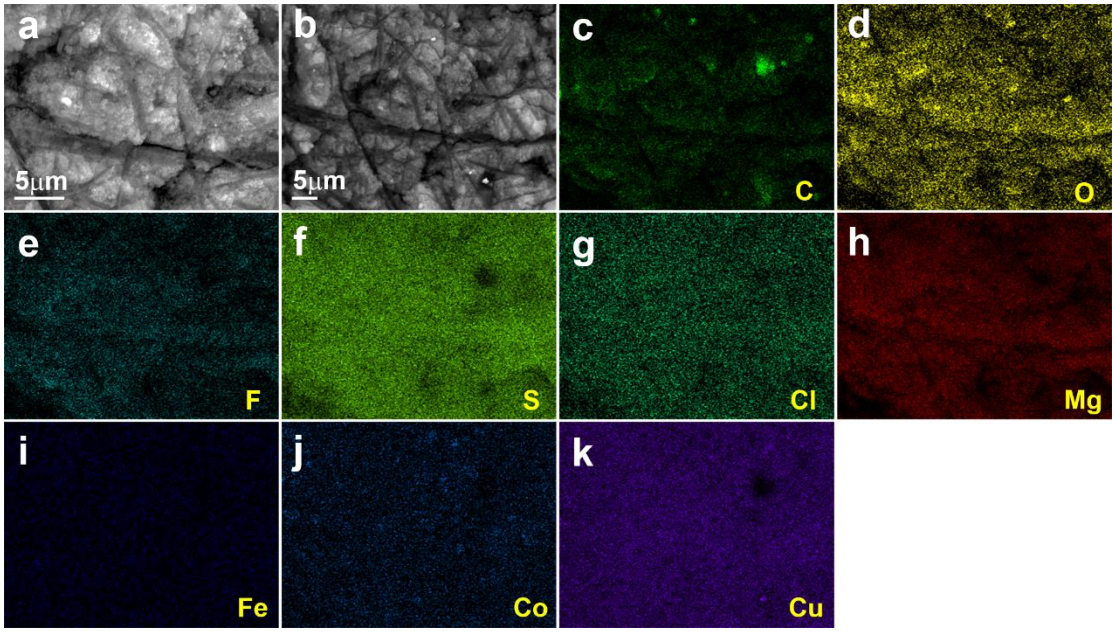

Figure S31. a, b) Typical SEM images at different magnifications of the $Fe_{0.5}Co_{0.5}S_2$ electrode in fully discharged state (cycle 50) and c-k) corresponding element mapping results.

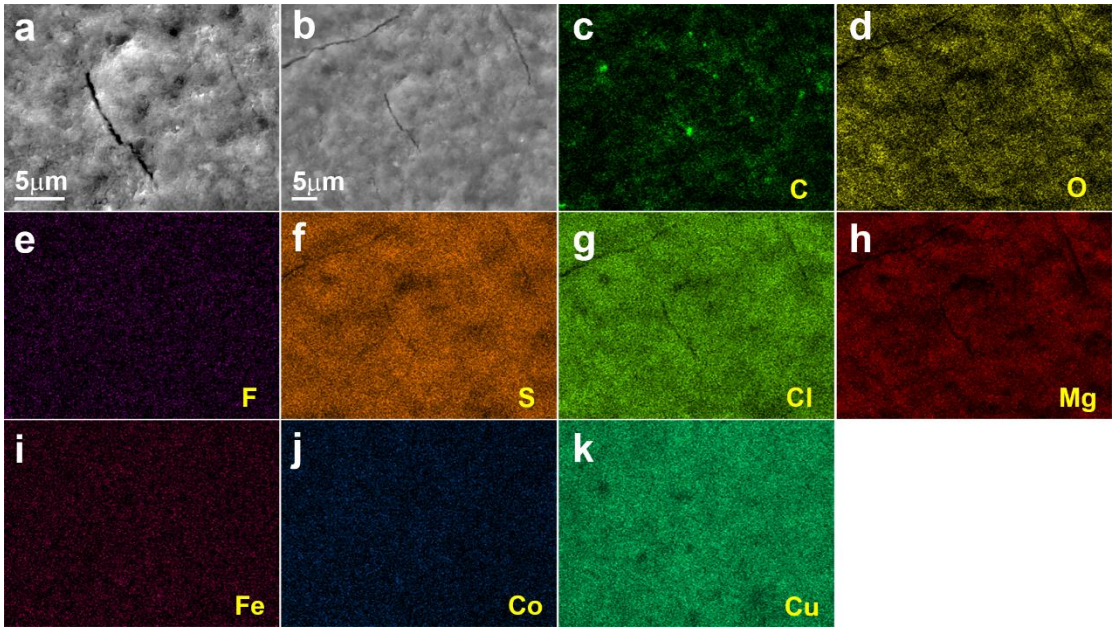

Figure S32. a, b) Typical SEM images at different magnifications of the $Fe_{0.5}Co_{0.5}S_2$ electrode in fully charged state (cycle 50) and c-k) corresponding element mapping results.

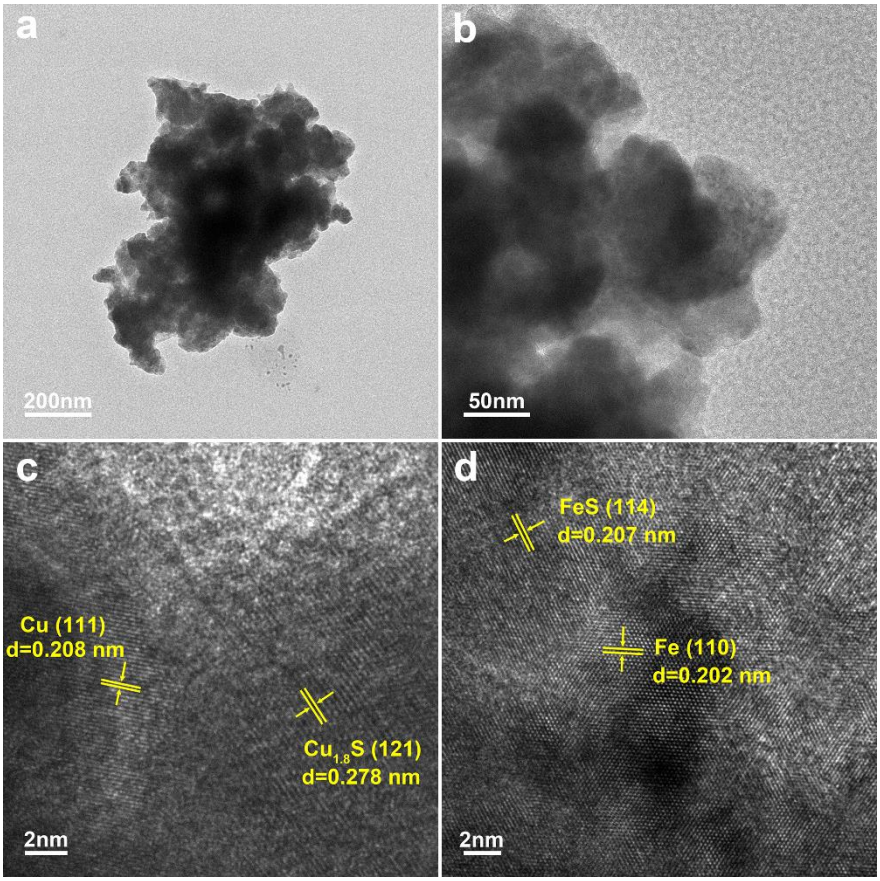

Figure S33. a, b) Typical TEM and c, d) HRTEM images of FeS_2 cathode in fully charged state (cycle 50).

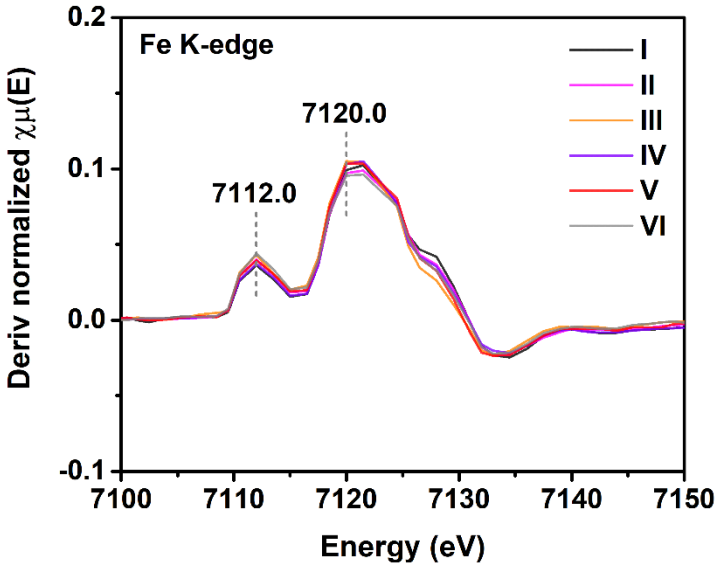

Figure S34. First-derivative XANES plots for FeS_2 cathodes in different states (I-VI) during 50^{th} cycle.

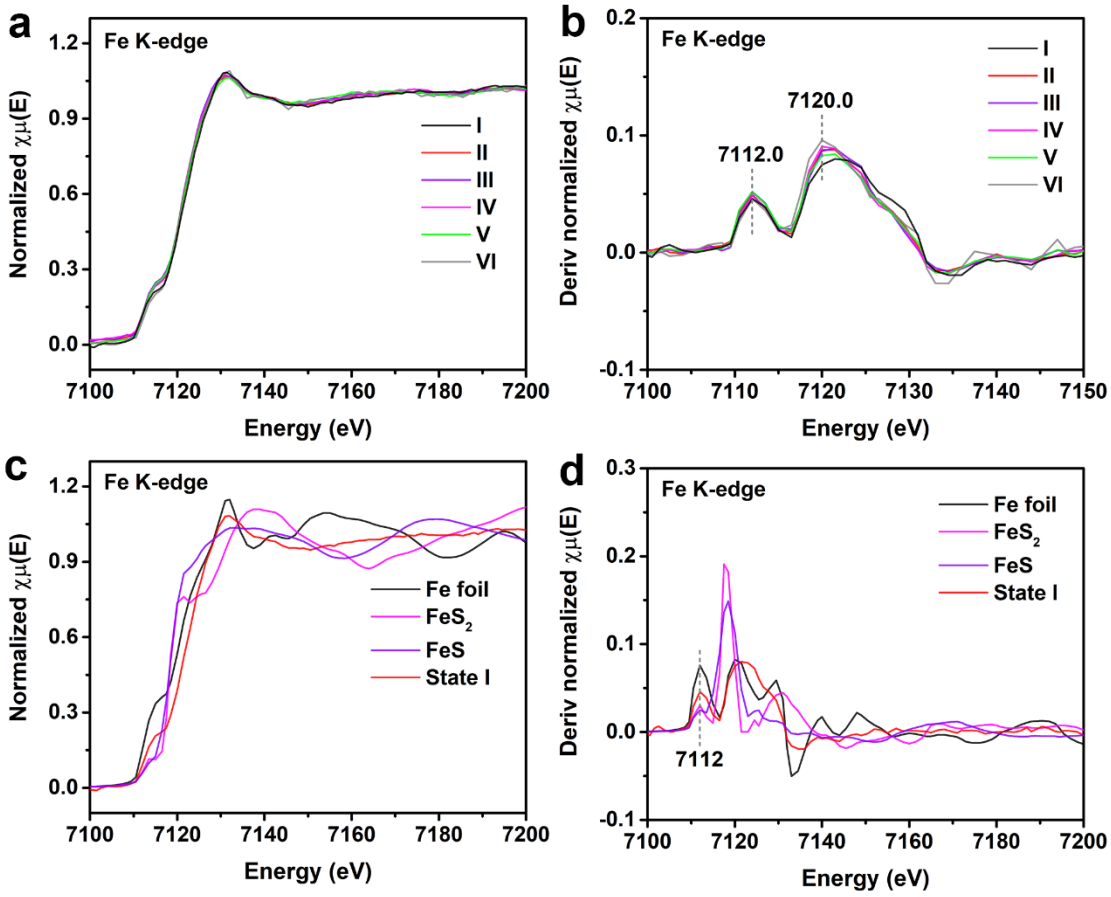

Figure S35. a) Fe K-edge XANES spectra and b) first-derivative XANES plots of $Fe_{0.5}Co_{0.5}S_2$ cathodes in different states (I-VI) during 50th cycle. c) Fe K-edge XANES spectra and d) first-derivative XANES plots of FeS_2, FeS, Fe foil and $Fe_{0.5}Co_{0.5}S_2$ cathode (state I).

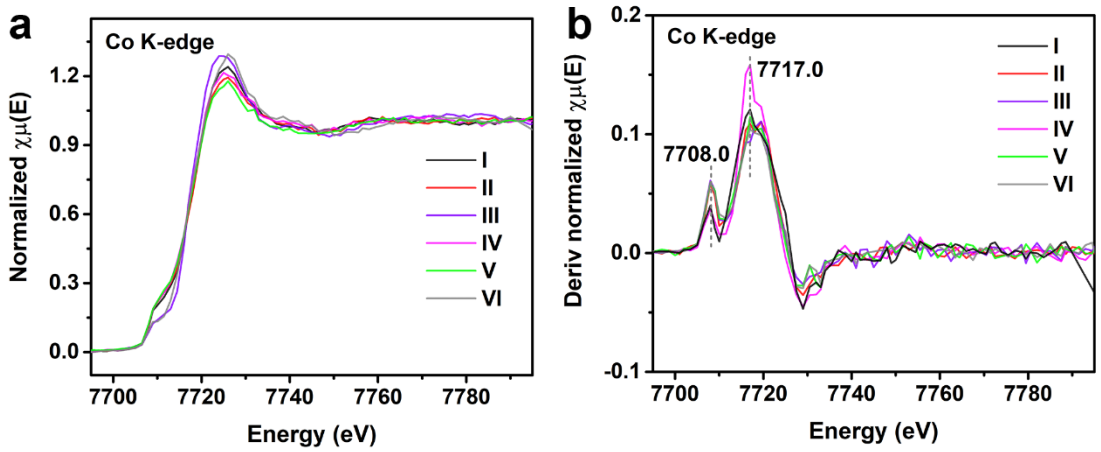

Figure S36. a) Co K-edge XANES spectra and b) first-derivative XANES plots of $Fe_{0.5}Co_{0.5}S_2$ cathodes in different states (I-VI) during 50^{th} cycle.

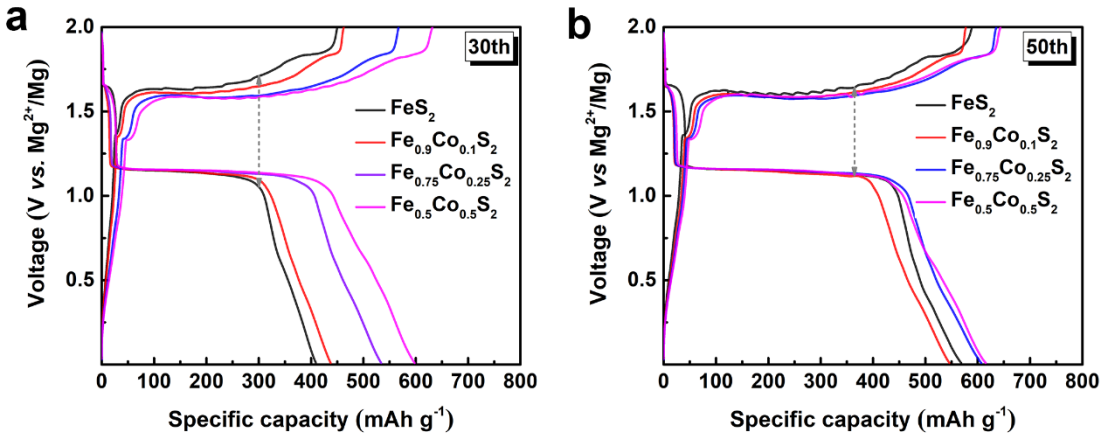

Figure S37. The discharge/charge profiles at 0.1 A g^{-1} of FeS_2, $Fe_{0.9}Co_{0.1}S_2$, $Fe_{0.75}Co_{0.25}S_2$ and $Fe_{0.5}Co_{0.5}S_2$ cathodes for RMBs during the a) 30^{th} and b) 50^{th} cycles.

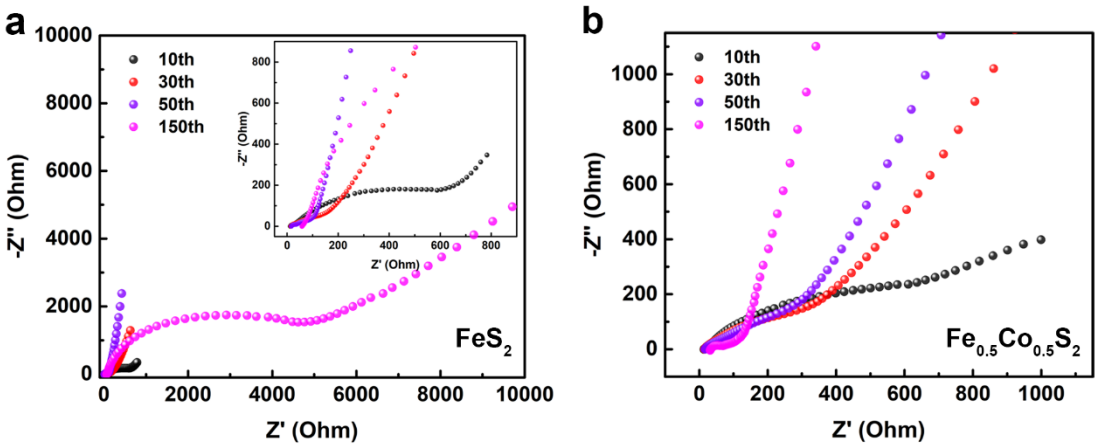

Figure S38. EIS of FeS_2 and $Fe_{0.5}Co_{0.5}S_2$ cathodes for RMBs after 10, 30, 50 and 150 cycles at 0.1 A g^{-1}.

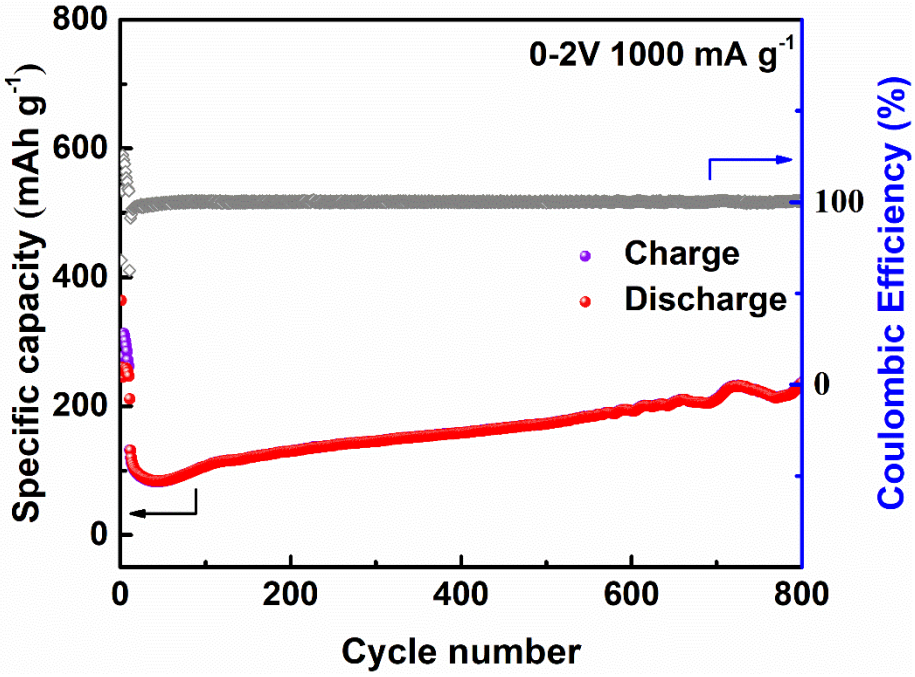

Figure S39. Cycling performance of sulfur cathodes at 1 A g^{-1} coupled with PMC electrolyte and copper collectors for RMBs.

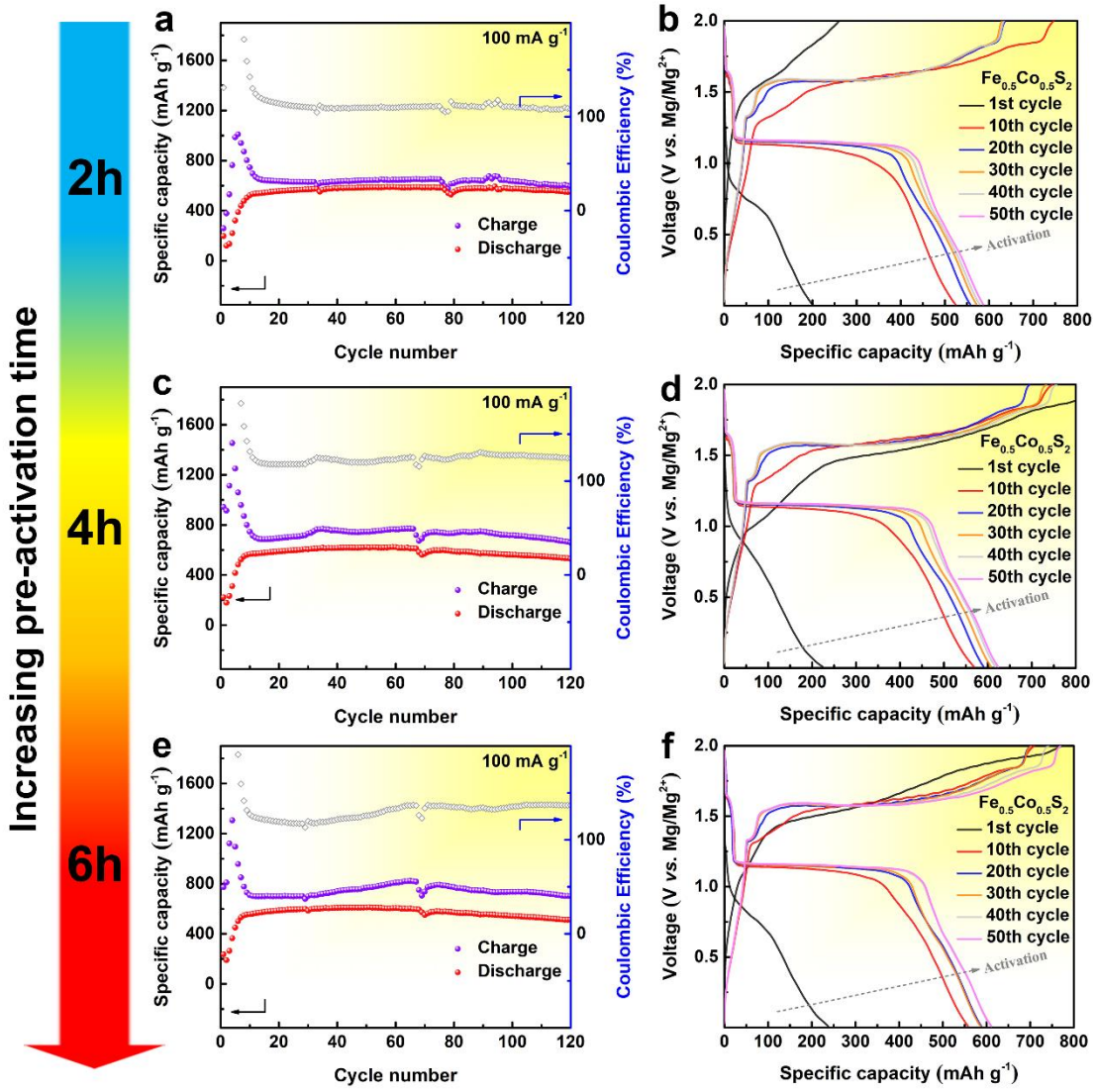

Figure S40. The cycling performance and corresponding discharge/charge profiles during the 1st, 10th, 20th, 30th, 40th and 50th cycles at 0.1 A g^{-1} of $Fe_{0.5}Co_{0.5}S_2$ cathodes coupling with PMC electrolyte and copper collectors for RMBs with pre-charging time of a, b) 2 h, c, d) 4 h and e, f) 6 h.

Supplementary tables

Table S1. Calculated sulfur (S) contents in typical metal sulfides and theoretical specific capacities based on full conversion reactions.

Samples	S content (wt. %)	Conversion Reactions	Theoretical specific capacity (TSC, mAh g^{-1})	$\frac{TSC_{sample}}{TSC_S}$ (%)
S	100.0	S+Mg↔MgS	1675	100.0
VS_4	71.6	VS_4+4Mg↔MgS+4V	1199	71.6
FeS_2	53.4	FeS_2+2Mg↔2MgS+Fe	894	53.4
CoS_2	52.1	CoS_2+2Mg↔2MgS+Co	873	52.1
NiS_2	52.2	NiS_2+2Mg↔2MgS+Ni	874	52.2
FeS	36.5	FeS+Mg↔MgS+Fe	611	36.5
CoS	35.2	CoS+Mg↔MgS+Co	589	35.2
NiS	35.3	NiS+Mg↔MgS+Ni	591	35.3
CuS	33.5	CuS+Mg↔MgS+Cu	561	33.5
Cu_2S	20.1	Cu_2S+Mg↔MgS+2Cu	336	20.1

Table S2. Available electrolytes for RMBs, their raw materials and estimated cost.

Electrolyte	Precursor	Materials Cost	Estimated price of 1mL electrolyte	Ref
0.3 M $Mg(HMDS)_2$-$(AlCl_3)_2$	$Mg(HMDS)_2$, $AlCl_3$	(1) $Mg(HMDS)_2$, 97 %: ¥23938/100 g. (2) $AlCl_3$: ¥671.5/100 g.	¥25.3	[10]
0.25 M $(MgCl_2)_2$-$AlCl_3$	$MgCl_2$, $AlCl_3$	(1) $MgCl_2$: ¥4794.4/100 g. (2) $AlCl_3$: ¥671.5/100 g.	¥2.4	[11]
$Mg(CB_{11}H_{12})_2$	$Cs(CB_{11}H_{12})_2$, $MgBr_2$, $AgNO_3$	(1) $Cs(CB_{11}H_{12})_2$: price not available. (2) $MgBr_2$, 98 %: ¥2952/100 g. (3) $AgNO_3$: ¥5532.6/100 g.	not available	[12]
0.05 M BCM	Boric Acid Tris(Hexafluoroisopropyl) Ester (THFPB), MgF_2	(1) THFPB, 95 %, TCI: ¥55000/100 g. (2) MgF_2: ¥1114.0/100 g.	¥563.3	[13]
0.3 M $Mg[B(HFIP)_4]_2$	$MgBH_4$, $(CF_3)_2CHOH$	(1) $MgBH_4$, 95 %:¥196020/100 g. (2) $(CF_3)_2CHOH$: ¥3778.9/100 g.	¥47.4	[14]
0.5 M $Mg(TFSI)_2$	$Mg(TFSI)_2$	$Mg(TFSI)_2$, 98 %:¥99980/100 g.	¥292.2	[15]
0.25 M $Mg(TFSI)_2$-$(MgCl_2)_2$	$Mg(TFSI)_2$, $MgCl_2$	(1) $Mg(TFSI)_2$, 98 %: ¥99980/100 g. (2) $MgCl_2$, ≥98 %: ¥4794.4/100 g.	¥148.4	[16]
0.25 M $Mg(TFSI)_2$-$(AlCl_3)_2$	$Mg(TFSI)_2$, $AlCl_3$	(1) $Mg(TFSI)_2$, 98%,¥99980/100 g. (2) $AlCl_3$: ¥671.5/100 g.	¥ 146.6	[17]
0.4 M $(PhMgCl)_2$-$AlCl_3$	PhMgCl, $AlCl_3$	(1) 2 M PhMgCl in THF: ¥880.9/100 mL. (2) $AlCl_3$: ¥671.5/100 g.	¥ 3.9	[9]
0.25 M $(R\text{-}PhOMgCl)_2$-$AlCl_3$	2-Tert-Butyl-4-Methylphenol (R-PhOH), CH_3CH_2MgCl, $AlCl_3$	(1) 2-Tert-Butyl-4-Methylphenol: ¥361.3/100 g. (2) 2 M CH_3CH_2MgCl in THF: ¥332.7/100 mL. (3) $AlCl_3$: ¥671.5/100 g.	¥ 1.4	This work

a. All chemical prices are from Sigma-Aldrich unless specified.
b. The price is normalized to ¥ /100 g or ¥ /100 mL.
c. The purity is >99 % or what is available.
d. The lowest price is chosen for chemicals.
e. The estimated price of 1 mL electrolyte is calculated without considering the solvent.
f. If the concentration and proportion of components in the electrolyte change, the estimated price of 1 mL electrolyte will change correspondingly.

Table S3. Electrochemical performance comparison of Co-doped FeS_2 with other typical cathode materials for RMBs reported in literatures corresponding to Figure 4o.

Cathode materials	Electrolytes	Voltage window (V vs. Mg)	Current density (mA g^{-1})	Capacities (mAh g^{-1})-(Cycle number)	Ref
Mo_6S_8	0.25 M $Mg(AlCl_2BuEt)_2$/THF	0.3-1.8	0.3 mA cm^{-2}	≈80 (580)	[18]
WSe_2	0.25 M $Mg(AlCl_2EtBu)_2$/THF	0.3-3.0	50	203 (160)	[19]
CoS	0.25 M $Mg(AlCl_2EtBu)_2$/THF	0.1-2	50	106 (60)	[20]
TiS_2	0.5 M $(PhMgCl)_2$-$AlCl_3$-Py14Cl/THF	0-2	240	≈120 (500)	[21]
$MgSn_2$	0.5 M PhMgCl/THF	0.01-0.6	16	≈200 (50)	[22]
$Ni_{0.75}Fe_{0.25}Se_2$	0.25 M $Mg(AlCl_2EtBu)_2$/THF	0.02-2.0	20	148 (500)	[23]
VS_4	0.4 M $(PhMgCl)_2$-$AlCl_3$/THF	0.2-2.2	100	150 (180)	[24]
			500	104 (500) 74 (800)	
α-Ag_2S/rGO	0.5 M $(PhMgCl)_2$-$AlCl_3$/THF	0.4-2	1000	46.3 (1000)	[25]
Mo_6S_8	0.4 M $(PhMgCl)_2$-$AlCl_3$/THF	0.5-2	64	89 (500)	[26]
$Ni_{0.85}Se$	0.2 M $Mg(HMDS)_2$-$(AlCl_3)_2$-$MgCl_2$/Diglyme	0-2.4	200	≈50 (500)	[27]
CuS-CTAB	0.3 M $Mg[B(hfip)_4]_2$/DME	0.01-2.4	100	≈360 (60)	[14]
			560	111 (1000)	
Bi nanosheets	0.25 M $(PhMgCl)_2$-$AlCl_3$/THF	0.05-0.6	200	297 (140)	[28]
MoS_2-infilled microcapsule	0.4 M $(PhMgCl)_2$-$AlCl_3$/THF	0.01-2.2	100	100 (100)	[29]
CuSe	0.3 M $Mg[B(hfip)_4]_2$/DME		200	180 (100)	[30]
			1000	47 (1000)	
FeS_2	0.3 M $Mg[B(hfip)_4]_2$/DME	0.01-2.4	50	600 (50)	[31]
			200	<200 (1000)	
Te-substituted CuS	0.3 M $Mg(HMDS)_2$-$(AlCl_3)_2$/DME	0.1-2.1	200	180 (80)	[10]
			500	115 (300) 43 (1500)	
Co-doped FeS_2	0.25 M $(R\text{-}PhOMgCl)_2$-$AlCl_3$/THF	0.01-2	100	698 (100)	This work
			200	522[a]	
			1000	249 (440)	
				164 (1000)	

a. The discharge capacity is obtained from rate performance corresponding to Figure

S21.

Table S4. The calculated lattice parameters by Rietveld refinement of XRD patterns.

Samples	a (Å)	b(Å)	c(Å)	α(°)	β(°)	γ(°)	Unit-cell volume ($Å^3$)	M-S(Å)	S-S(Å)	Bragg R-factor	RF-factor
FeS_2	5.4420	5.4420	5.4420	90	90	90	161.1668	2.2874	2.053	7.87	4.15
$Fe_{0.9}Co_{0.1}S_2$	5.4359	5.4359	5.4359	90	90	90	160.6255	2.2861	2.040	6.58	3.05
$Fe_{0.75}Co_{0.25}S_2$	5.4485	5.4485	5.4485	90	90	90	161.7450	2.2940	2.023	9.73	4.55
$Fe_{0.5}Co_{0.5}S_2$	5.4601	5.4601	5.4601	90	90	90	162.7803	2.2971	2.043	8.90	4.07

Table S5. EDX results (at%) of of FeS_2, $Fe_{0.9}Co_{0.1}S_2$, $Fe_{0.75}Co_{0.25}S_2$ and $Fe_{0.5}Co_{0.5}S_2$ samples.

Samples	Fe	Co	S
FeS_2	32.8	0	67.2
$Fe_{0.9}Co_{0.1}S_2$	30.8	3.5	65.7
$Fe_{0.75}Co_{0.25}S_2$	26.5	8.6	64.9
$Fe_{0.5}Co_{0.5}S_2$	15.0	18.5	66.5
$Fe_{0.25}Co_{0.75}S_2$	11.2	28.8	60.0
$Fe_{0.1}Co_{0.9}S_2$	3.7	35.5	60.8

Table S6. The BET surface areas of samples determined by N_2 adsorption and desorption isotherms.

Samples	**BET surface area ($m^2 g^{-1}$)**
FeS_2	2
$Fe_{0.9}Co_{0.1}S_2$	5
$Fe_{0.75}Co_{0.25}S_2$	9
$Fe_{0.5}Co_{0.5}S_2$	23

Table S7. Curve fit parameters[a] for Fe K-edge EXAFS of FeS_2.

Path	d[b]/Å	N	R/Å	Sigma^2
Fe-S1	2.2624	6	2.2552	0.0053
Fe-S2	3.4538	6	3.4538	0.9530
Fe-Fe	3.8310	12	3.8310	0.7270

[a]S_0^2 was fixed as 0.83. ΔE_0 was refined as a global fit parameter, returning a value of 0.99 eV. Data ranges: 2<k<11.45 Å^{-1}, 1<R<6 Å. The number of parameters is 10, out of a total of 30 independent data points. R factor for this fit is 0.63 %. [b]The distances for Fe-S, Fe-Fe are from the FEFF file of FeS_2.

Table S8. Curvefit parameters[a] for Co K-edge EXAFS of CoS_2.

Path	d[b]/Å	N	R/Å	Sigma^2
Co-S1	2.3237	6	2.3105	0.00495
Co-S2	3.4851	6	3.4284	0.01197
Co-Co	3.9137	12	3.9097	0.01228

[a]S_0^2 was fixed as 0.72. ΔE_0 was refined as a global fit parameter, returning a value of 2.69 eV. Data ranges: 2<k<10 Å^{-1}, 1<R<6 Å. The number of parameters is 10, out of a total of 25 independent data points. R factor for this fit is 0.3 %. [b]The distances for Co-S, Co-Co are from the FEFF file of CoS_2.

Table S9. EDX results (wt%) of FeS_2 electrode in different states.

State	C	O	F	S	Cl	Mg	Fe	Cu	total	Mg/S
pristine	53.8	2.72	1.02	19.68			20.98	1.81	100.0	
50th-dis	20.34	8.25	1.24	15.40	1.16	12.52	0.61	40.47	100.0	0.813
50th-ch	18.27	5.16	0.81	13.59	1.55	4.17	0.59	55.85	100.0	0.307

Table S10. EDX results (wt%) of FeS_2 electrode in different states.

State	C	O	F	S	Cl	Mg	Fe	Co	Cu	total	Mg/S
pristine	36.47	5.14	1.79	21.53			10.51	11.11	13.45	100.0	
50th-dis	31.54	9.2	2.65	11.99	1.3	9.14	0.57	2.06	31.54	100.0	0.762
50th-ch	22.02	9.18	1.55	8.99	11.01	3.69	0.33	1.14	42.1	100.0	0.410

References

[1] a) D. Aurbach, R. Turgeman, O. Chusid, Y. Gofer, *Electrochem. Commun.* **2001**, *3*, 252; b) I. T. Kim, K. Yamabuki, M. Sumimoto, H. Tsutsumi, M. Morita, N. Yoshimoto, *J. Power Sources* **2016**, *323*, 51.

[2] K. Sato, G. Mori, T. Kiyosu, T. Yaji, K. Nakanishi, T. Ohta, K. Okamoto, Y. Orikasa, *Sci. Rep.* **2020**, *10*, 7362.

[3] D. Aurbach, M. Moshkovich, A. Schechter, R. Turgeman, *Electrochem. Solid-State Lett.* **2000**, *3*, 31.

[4] T. Pavcnik, M. Lozinsek, K. Pirnat, A. Vizintin, T. Mandai, D. Aurbach, R. Dominko, J. Bitenc, *ACS Appl. Mater. Interfaces* **2022**, DOI: 10.1021/acsami.2c05141.

[5] O. Mizrahi, N. Amir, E. Pollak, O. Chusid, V. Marks, H. Gottlieb, L. Larush, E. Zinigrad, D. Aurbach, *J. Electrochem. Soc.* **2008**, *155*, A103.

[6] Y. Cheng, R. M. Stolley, K. S. Han, Y. Shao, B. W. Arey, N. M. Washton, K. T. Mueller, M. L. Helm, V. L. Sprenkle, J. Liu, G. Li, *Phys. Chem. Chem. Phys.* **2015**, *17*, 13307.

[7] a) C. Liao, B. Guo, D.-e. Jiang, R. Custelcean, S. M. Mahurin, X.-G. Sun, S. Dai, *J. Mater. Chem. A* **2014**, *2*, 581; b) B. Pan, J. Zhang, J. Huang, J. T. Vaughey, L. Zhang, S. D. Han, A. K. Burrell, Z. Zhang, C. Liao, *Chem. Commun.* **2015**, *51*, 6214; c) B. Pan, J. Huang, N. Sa, S. M. Brombosz, J. T. Vaughey, L. Zhang, A. K. Burrell, Z. Zhang, C. Liao, *J. Electrochem. Soc.* **2016**, *163*, A1672.

[8] a) E. G. Nelson, J. W. Kampf, B. M. Bartlett, *Chem. Commun.* **2014**, *50*, 5193; b) A. J. Crowe, B. M. Bartlett, *J. Mater. Chem. A* **2016**, *4*, 368.

[9] N. Pour, Y. Gofer, D. T. Major, D. Aurbach, *J. Am. Chem. Soc.* **2011**, *133*, 6270.

[10] Y. Cao, Y. Zhu, C. Du, X. Yang, T. Xia, X. Ma, C. Cao, *ACS Nano* **2022**, *16*, 1578.

[11] R. Doe, R. Han, J. Hwang, A. Gmitter, I. Shterenberg, H. Yoo, N. Pour, D. Aurbach, *Chem. Commun.* **2014**, *50*, 243.

[12] O. Tutusaus, R. Mohtadi, T. Arthur, F. Mizuno, E. Nelson, Y. Sevryugina, *Angew. Chem. Int. Ed.* **2015**, *54*, 7900.

[13] Z. Zhang, Z. Cui, L. Qiao, J. Guan, H. Xu, X. Wang, P. Hu, H. Du, S. Li, X. Zhou, S. Dong, Z. Liu, G. Cui, L. Chen, *Adv. Energy Mater.* **2017**, *7*, 1602055.

[14] Y. Shen, Y. Wang, Y. Miao, M. Yang, X. Zhao, X. Shen, *Adv. Mater.* **2020**, *32*, 1905524.

[15] N. Singh, T. S. Arthur, C. Ling, M. Matsui, F. Mizuno, *Chem. Commun.* **2013**, *49*, 149.

[16] I. Shterenberg, M. Salama, H. Yoo, Y. Gofer, J. Park, Y. Sun, D. Aurbach, *J. Electrochem, Soc*, **2015**, *162*, A7118.

[17] H. Xu, X. Zhang, T. Xie, Z. Li, F. Sun, N. Zhang, H. Chen, Y. Zhu, X. Zou, C. Lu, J. Zou, R. M. Laine, *Energy Stor. Mater.* **2022**, *46*, 583.

[18] D. Aurbach, Z. Lu, A. Schechter, Y. Gofer, H. Gizbar, R. Turgeman, Y. Cohen, M. Moshkovich, E. Levi, *Nature* **2000**, *407*, 724-727.
[19] B. Liu, T. Luo, G. Mu, X. Wang, D. Chen, G. Shen, *ACS Nano* **2013**, *7*, 8051.
[20] D. He, D. Wu, J. Gao, X. Wu, X. Zeng, W. Ding, *J. Power Sources* **2015**, *294*, 643..
[21] H. D. Yoo, Y. Liang, H. Dong, J. Lin, H. Wang, Y. Liu, L. Ma, T. Wu, Y. Li, Q. Ru, Y. Jing, Q. An, W. Zhou, J. Guo, J. Lu, S. T. Pantelides, X. Qian, Y. Yao, *Nat. Commun.* **2017**, *8*, 339.
[22] D. T. Nguyen, S. W. Song, *J. Power Sources* **2017**, *368*, 11.
[23] L. Zhou, F. Xiong, S. Tan, Q. An, Z. Wang, W. Yang, Z. Tao, Y. Yao, J. Chen, L. Mai, *Nano Energy* **2018**, *54*, 360.
[24] Y. Wang, Z. Liu, C. Wang, X. Yi, R. Chen, L. Ma, Y. Hu, G. Zhu, T. Chen, Z. Tie, J. Ma, J. Liu, Z. Jin, *Adv. Mater.* **2018**, *30*, 1802563.
[25] Z. Chen, Z. Zhang, A. Du, Y. Zhang, M. Men, G. Li, G. Cui, *Chem. Commun.* **2019**, *55*, 4431.
[26] M. Mao, Z. Lin, Y. Tong, J. Yue, C. Zhao, J. Lu, Q. Zhang, L. Gu, L. Suo, Y. S. Hu, H. Li, X. Huang, L. Chen, *ACS Nano* **2020**, *14*, 1102.
[27] D. Chen, J. Shen, X. Li, S. Cao, T. Li, W. Luo, F. Xu, *J. Energy Chem.* **2020**, *48*, 226.
[28] X. Xu, D. Chao, B. Chen, P. Liang, H. Li, F. Xie, K. Davey, S. Qiao, *Angew. Chem. Int. Ed.* **2020**, *59*, 21728.
[29] X. Lin, J. Liu, H. Zhang, Y. Zhong, M. Zhu, T. Zhou, X. Qiao, H. Zhang, T. Han, J. Li, *Adv. Sci.* **2021**, *8*, 2002298.
[30] Y. Zhang, Y. Zhu, Z. Wang, H. Peng, X. Yang, Y. Cao, C. Du, X. Ma, C. Cao, *Adv. Funct. Mater.* **2021**, *31*, 2104730.
[31] Y. Shen, Q. Zhang, Y. Wang, L. Gu, X. Zhao, X. Shen, *Adv. Mater.* **2021**, *33*, 2103881.